ARMY RESEARCH LABORATORY

In-Flight Projectile Imaging by Infrared Emission/Rotating Mirror Technique With Temperature Calibration

Charles R. Stumpfel

ARL-TR-1148 JULY 1996

The findings in this report are not to be construed as an official Department of the Army position unless so designated by other authorized documents.

Citation of manufacturer's or trade names does not constitute an official endorsement or approval of the use thereof.

Destroy this report when it is no longer needed. Do not return it to the originator.

REPORT DOCUMENTATION PAGE

Form Approved
OMB No. 0704-0188

1. AGENCY USE ONLY *(Leave blank)*	2. REPORT DATE	3. REPORT TYPE AND DATES COVERED
	July 1996	Final

4. TITLE AND SUBTITLE

In-Flight Projectile Imaging by Infrared Emission/Rotating Mirror Technique With Temperature Calibration

5. FUNDING NUMBERS

PR: 1L162618AH80

6. AUTHOR(S)

Stumpfel, C. R.

7. PERFORMING ORGANIZATION NAME(S) AND ADDRESS(ES)

U.S. Army Research Laboratory
Weapons Technology Directorate
Aberdeen Proving Ground, MD 21010-5066

8. PERFORMING ORGANIZATION REPORT NUMBER

9. SPONSORING/MONITORING AGENCY NAME(S) AND ADDRESS(ES)

U.S. Army Research Laboratory
Weapons Technology Directorate
Aberdeen Proving Ground, MD 21010-5066

10. SPONSORING/MONITORING AGENCY REPORT NUMBER

ARL-TR-1148

11. SUPPLEMENTARY NOTES

12a. DISTRIBUTION/AVAILABILITY STATEMENT

Approved for public release; distribution is unlimited.

12b. DISTRIBUTION CODE

13. ABSTRACT *(Maximum 200 words)*

Many projectiles experience considerable heating which begins with the launch process in the gun and continues with aerodynamic heating throughout the flight. The high temperatures that result cause the surface to emit considerable infrared radiation. In this work, a rotating mirror system was applied to image projectiles by infrared emission. Factors that affect this system's image quality are identified and described. In addition to imaging, infrared emission may also be used to measure the surface temperatures of projectile components. A technique was developed to calibrate the system for measuring surface temperature. The surface temperature distribution on a tank-fired 120-mm M865 training projectile, with velocity of 1600 m/sec, was measured and is displayed in the report.

14. SUBJECT TERMS

aerodynamic heating
projectile infrared emission
projectile signature measurement
projectile temperature measurement
rotating mirror

15. NUMBER OF PAGES

100

16. PRICE CODE

17. SECURITY CLASSIFICATION OF REPORT	18. SECURITY CLASSIFICATION OF THIS PAGE	19. SECURITY CLASSIFICATION OF ABSTRACT	20. LIMITATION OF ABSTRACT
Unclassified	Unclassified	Unclassified	

INTENTIONALLY LEFT BLANK

ACKNOWLEDGMENTS

The author would like to thank several ARL project test engineers for accommodating the imaging experiments during their gun system or projectile tests, and in particular, Frederick Brandon, Mark Bundy, Richard Pennekamp, Douglas Savick, and Raymond Von Wahlde.

Peter Plostins, Keith Soencksen, and George Thomson of ARL made available, guided, and supported the M865 tests. The purpose of these tests was the measurement of projectile surface temperature distributions. Bernard Guidos, ARL, applied computational fluid dynamics to calculate projectile surface temperatures. These results were useful in selecting the projectile for the temperature measurement tests.

We have often benefitted from the high level of knowledge, in ballistic technology and firing range instrumentation, and the excellent operational skills of the personnel in ARL's Transonic Range at APG. In particular, we mention Edmond Baur, Albert Bowers, James Foley, James Garner, John Heath, Barry Hudler, Robert Keppinger, Vural Oskay, and Kenneth Willan.

The most important and costly component of the rotating mirror system, the PtSi IR imager, was generously made available by Richard Beyer, ARL.

Within the Survivability Concepts Branch, the laboratory's infrastructure and experimental activities receive very substantial contributions from Keith Mahan, Frederick Pierce, and Steven Rogers. In particular, the author acknowledges the many contributions of Joseph Correri in these areas and especially for this experimental activity. Andrus Niiler and George Thomson discussed the manuscript and contributed many valuable suggestions.

The manuscript was technically reviewed by James Rapp, ARL. Several suggestions were made which led to significant improvements in the report. The report received an editorial review by Nancy Ryan, ARL, and again, many improvements were made.

INTENTIONALLY LEFT BLANK

TABLE OF CONTENTS

INTENTIONALLY LEFT BLANK

LIST OF FIGURES

INTENTIONALLY LEFT BLANK

LIST OF TABLES

INTENTIONALLY LEFT BLANK

IN-FLIGHT PROJECTILE IMAGING BY INFRARED EMISSION/ROTATING MIRROR TECHNIQUE WITH TEMPERATURE CALIBRATION

1. INTRODUCTION

In general, all gun-launched high velocity projectiles are subject to significant heating first in the launch process and then by aerodynamic heating throughout the flight. Conventional powder guns, which have been developed for hundreds of years, have continued to improve performance by increasing the temperature and pressure of the gun systems. More recent research has been aimed at launching projectiles at higher velocities by applying new launching technologies based, for example, on electrothermal-chemical or electromagnetic principles. Each method of accelerating the projectile will have significantly different heating phenomenology.

Conventional powder guns such as those employed in tanks often launch subcaliber projectiles, which are accelerated by sabots. While the projectile is being accelerated in the gun tube, its rearward components, which are not covered by the sabots, are heated by contact with hot propellant gases at peak pressures as high as 80,000 lb/in^2 and with temperatures as great as about 3200 K [1]. After the projectile exits the gun, aerodynamic heating occurs on its entire surface. High rates of heat transfer are present on some of the projectile's surfaces such as those of the nose and the leading edges of fins. In addition, if a tracer is present inside the fin assembly, it also will contribute heating.[1] For large caliber tank-fired projectiles, the duration of the in-bore launch heating is about 0.01 second and the duration of the in-flight aerodynamic heating is a few seconds.

The temperature distribution produced by the high heating rates is an important consideration in designing projectiles and one that will become more critical as velocity is increased. The temperatures that are encountered may cause the materials of the nose, fins, or other components of the aerodynamic body to lose strength, melt, or ablate and adversely affect the projectile flight. Heat-loading problems seem especially important today for very high velocity projectiles that have thin fins made of aluminum alloy. In recognition of these issues, in recent years considerable experimental [1] and theoretical research [2-4] has been directed toward understanding the thermal stresses on the components of high velocity projectiles both in the launch and flight phases. The computation of aerothermal heating and projectile surface temperatures is a problem of special interest in the area of computational fluid dynamics (CFD).

[1]An attempt to find publications giving the magnitude of tracer heating was not successful. Subsequently, a simple tracer burn test was done and is discussed in Appendix A.

The elevated surface temperatures on high velocity projectiles will result in the strong emission of infrared radiation. Infrared (IR) radiation may be measured and the temperature distribution on the projectile surface may be inferred. The basic techniques of thermography are well advanced [7], but applications involving temperature distribution measurements on in-flight high velocity projectiles have not become practical.

In addition to measuring projectile temperatures, IR radiation may also be used to find the projectile for tracking. Projectile tracking may be useful for any number of applications, one of which is the self-protection of armored vehicles.

The objective of this work is to understand the phenomenology of IR emission from high velocity projectiles and to apply the knowledge to tracking projectiles for self-protection of armored vehicles. To obtain this objective, it is first necessary to develop instrumentation that can be used to gather data about projectile IR emission. This instrumentation may also be used to measure projectile surface temperature distributions.

This report describes a rotating mirror system for acquiring IR projectile images and the calibration of the images to show projectile surface temperature. The speed of the rotating mirror can be set so that the imager remains pointed at the moving projectile, and thereby, a stationary image is produced in the IR imager. After acquiring the image of an in-flight projectile, the infrared system's exposure time and optical collection characteristics as they existed for the in-flight recording were determined. A technique employing an IR reference source with a chopper was used to perform temperature calibration of the recorded projectile images.

The experiments so far have involved only saboted projectiles launched from 105- and 120-mm tank guns. To the present, most projectile images were collected during tests conducted for other purposes and are not calibrated to provide surface temperature. The signal levels in these uncalibrated images do, however, give some indication of relative temperatures between adjacent surface areas. For example, the signals may be used to find hot spots on the surface. These images are useful for qualitative understanding of projectile heating phenomenology.

Five M865 training projectiles have been fired in tests that were conducted for temperature measurement. For these tests, a temperature calibration procedure was applied which involved both laboratory measurements on a projectile model and calibration of the system as used in the field. The field calibration procedure required a few hours and was done only after images with suitable signal levels were recorded.

This experimental work has resulted in (a) the development of a technique for imaging in-flight projectiles by IR emission; (b) the capture of many IR projectile images that are uncalibrated for temperature; (c) the development of a technique for calibrating the images to indicate the surface temperature distribution; and (d) the capture of one emission image of an M865 projectile, which was calibrated for temperature and displayed with colors to indicate temperature.

The image quality of the rotating mirror system is an important issue since observation of the temperature distribution on projectile surfaces is limited by the spatial resolution of the system. For example, to be accurately measured, the spatial features of the temperature distribution must be larger than the spatial resolution limitations of the IR imaging system. Several phenomena contribute to image blur when the rotating mirror system is used to image high velocity projectiles. These blur-inducing phenomena were identified and described, and approaches to reduce image blur are given.

In addition, the issue of which IR imagers may be useful for rotating mirror or other projectile emission thermography was examined in a laboratory screening test. The threshold temperatures required to produce usable signals were measured for five imagers available in this laboratory as follows:

1. Pyroelectric imager, 1.8 to 14 μm
2. Platinum silicide (PtSi) imager, 1.8 to 5.5 μm
3. Near IR vidicon camera, PbO-PbS, 0.9 to 2.5 μm
4. CCD camera, 0.4 to 1.1 μm
5. Infrared film, as used in a firing range streak camera, 0.4 to 0.9 μm.

Imager descriptions, experimental conditions, and results are presented in Appendix B.

The report describes in detail the rotating mirror system and its calibration for temperature measurement of in-flight projectiles. It includes, as an example of the instrument's performance, the image of a M865 projectile image with temperature distribution indicated.

2. INSTRUMENTATION

2.1 Projectile Imaging by Velocity Compensation with a Rotating Mirror

Early applications of rotating mirrors to projectile imaging were made by personnel of the Royal Armaments Research and Development Establishment (RARDE), Fort Halstead, England, using a system called the "flight follower" [discussed in Ref. 5]. More recently, a system called the "projectile follower system" is being developed at the Aberdeen Test Center (formerly Combat Systems Test Activity), Aberdeen Proving Ground [5]. This system uses a computer to keep a mirror pointing at in-flight projectiles. The rotation rate versus time is programmable before the shot, based on predicted projectile velocity. The mirror is initially at rest and, when triggered by the projectile, rotates up to speed with high angular acceleration rates. The system's variable rotation rate allows it to follow the projectile over a considerable length of the trajectory, i.e., about 200 meters. Observations over this length of trajectory are essential for showing the projectile's mechanical condition and orientation, which are of particular interest just after sabot discard. The "projectile follower system" has used video cameras and high speed film cameras with frame rates of thousands per second. The video and film cameras operate in the visible part of the spectrum.

In this work, a rotating mirror was used for IR imaging. This rotating mirror has a constant rotation rate and detects the projectile at just one location on the trajectory (from a viewpoint that lies perpendicular to the trajectory). The IR observations provide either an IR emission image or, when calibrated, the projectile's surface temperature distribution at one range from the gun.

This section includes a general description of the rotating mirror system but does not consider issues of image quality. In the subsequent section, the system is analyzed for image quality by examining sources of image blur.

To image a high velocity projectile with a stationary imager, a means of compensating for the projectile velocity is necessary (in this case, from 1 to 2 km/sec) while the imager collects photons. A rotating mirror system can be applied to stabilize the image of the in-flight projectile. As a source element on the projectile travels along the trajectory, IR rays from the source reach the mirror's surface with slightly changing angles of incidence as shown by the sample rays on Figures 1 and 2. When the mirror is set to the proper rotation rate, however, the reflection leaving the mirror to go to the imager's lens will not change direction during the exposure. The

image falling on the imager's detector array is then held stationary. (Producing a stationary image from a moving projectile is often referred to as "motion compensation.")

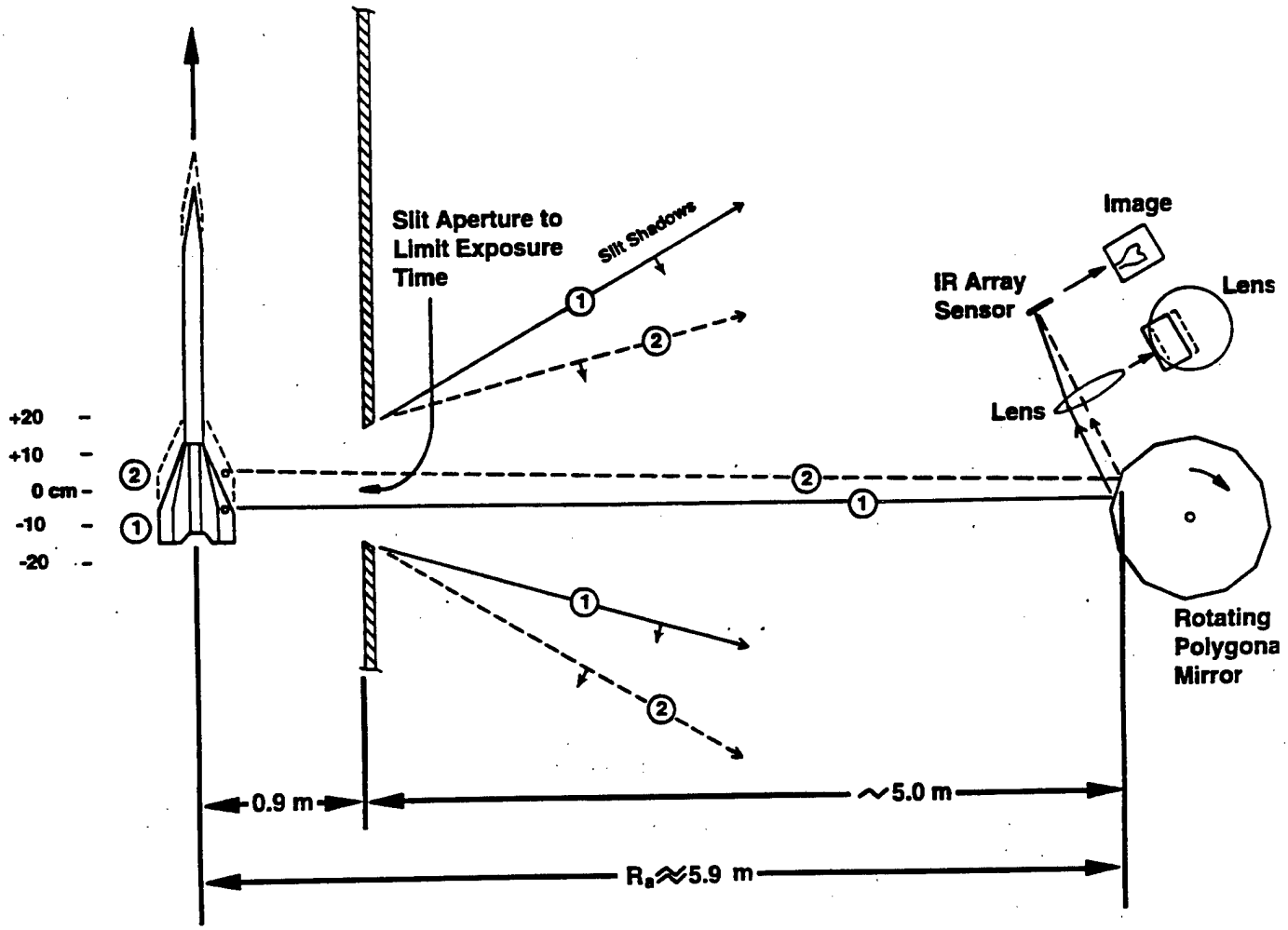

Figure 1. Rotating Mirror Setup for Projectile Imaging.

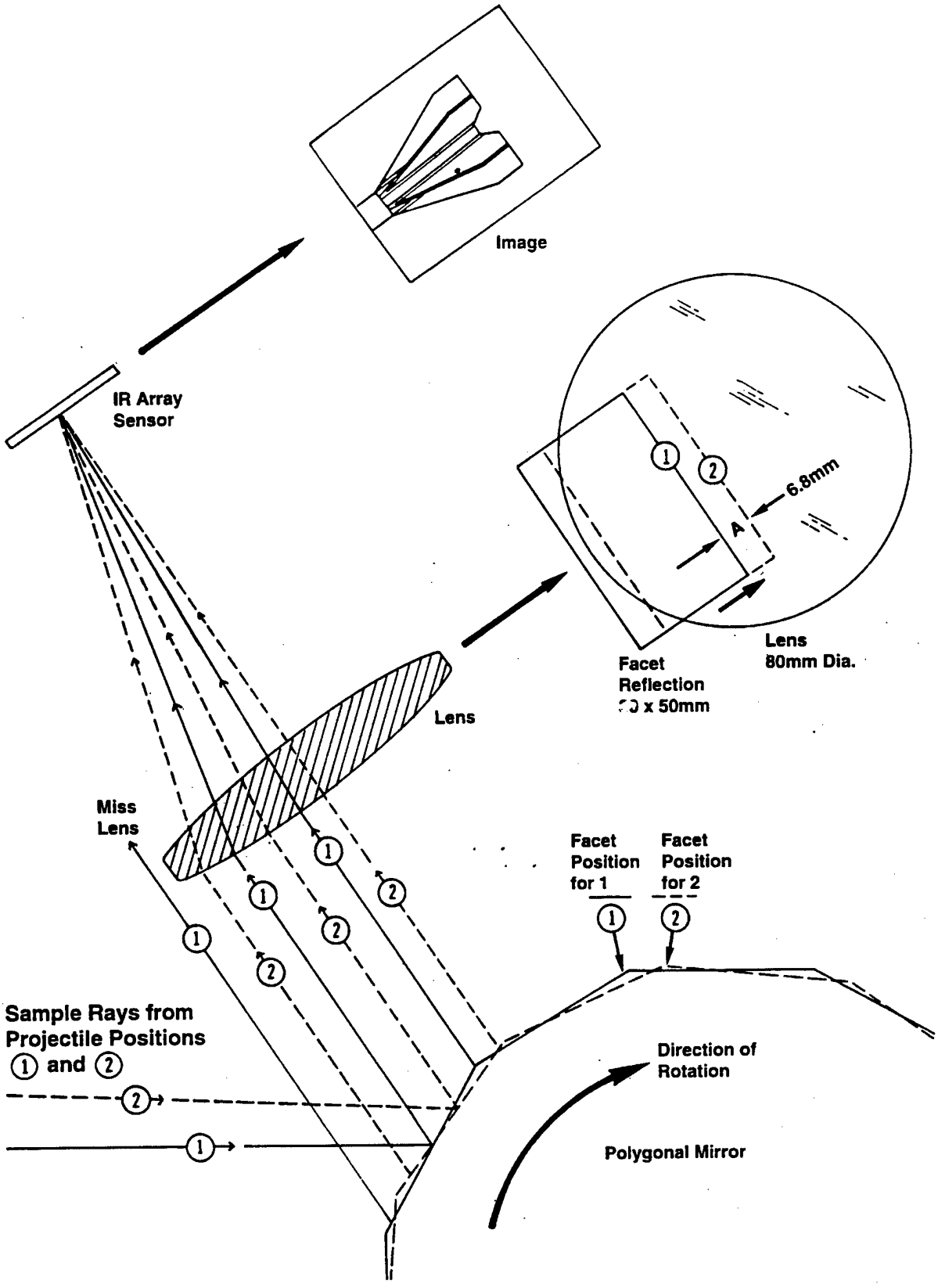

Figure 2. Close-Up of Mirror and IR Imager. (Mirror-lens vignetting is shown.)

When an imager views a plane mirror which is rotating with an angular rate of ω, the field of view (FOV) of the imager rotates with an angular rate of 2ω. At a distance, R, from the mirror a point in the imager FOV translates with a velocity, V_m, of

$$V_m = 2\omega R. \tag{1}$$

For a projectile on a trajectory located R_a from the mirror, the projectile's image will be stationary when the projectile velocity, V_a, equals the FOV velocity, V_{ma},

$$V_a = V_{ma},$$

$$V_a = 2\omega_a R_a. \tag{2}$$

Subscript a, in V_a, R_a, and ω_a indicates the actual value realized in a test. Subscript p, in V_p, R_p, and ω_p used in the later discussion, indicates predicted values used, for example, before a test to determine the rotation rate setting of the mirror.

The mirror used for imaging is a single facet on a polygonal mirror of 20 facets. The distance between opposing facets is 20 cm. Each facet, which is the system's limiting aperture, is 3 cm wide by 5 cm high. The polygon is driven by a brushless DC motor.[2] For a typical setup, with the system placed 6 meters off the trajectory, the rotation rate required to "freeze" the image of a projectile with a velocity of 1500 meters/second is about 20 revolutions per second (rps).

To limit the exposure time, a slit is placed close to the trajectory so that a radiating element on the projectile surface can be observed only over a limited distance or time. The slit blocks most of the trajectory, but as the projectile approaches, it reaches a point where the slit edge first allows light to reach the mirror facet, thereby starting the exposure time. Farther along the trajectory, the second slit edge blocks the light to end the exposure time. The rays marked "slit shadows" in Figure 1 show the location of these "shadow" rays which pass across the facet to start and stop the exposure time. For the case shown, the shadow rays indicate no slit blockage of the mirror facet and light is fully transmitted from Locations 1 and 2.

This system has optical characteristics that vary with time and require consideration in calibrating for temperature measurements. The mirror's rotational position is random, or unsynchronized, with respect to the projectile's location on the trajectory. Therefore, when the

[2]The polygonal mirror, motor, and controller were manufactured by Multi-Scanning Devices Corp.

projectile appears behind the slit, the angular orientation of the mirror will be random and will show variation from shot to shot. The light reflected from the facet will then have an initial random location upon entering the lens aperture. Figure 2 shows the facet's angular orientation and the path of the reflected rays as they enter the lens. In addition, during the exposure time as the polygon rotates, the facet translates a few millimeters and the reflected light will therefore translate across the lens aperture. This translation at the lens is indicated by "**A**" on Figure 2. The IR radiation will be partially blocked (or vignetted) whenever it strikes the edge of the lens aperture. Also, if the projectile crosses the slit when the mirror is oriented so that the reflection misses the lens entirely, then the projectile is not detected. In these tests, the time a source element could radiate to the rotating mirror was shorter than the time it takes the facet's reflection to cross the lens. For example, in one setup the slit limited the exposure time to about 300 μsec while the time for a facet reflection to cross the lens was about 2 msec. (An exposure time of 300 μsec is too long for sharp imaging, as will be discussed.) The calibration technique takes into account lens and other system vignetting which may have occurred during in-flight test recordings by making measurements after the shot, as described later.

The exposure time can be determined by examining the length of the trajectory, l_a, as limited by the slit, along which the projectile can be observed. For setups with larger slits, for example, with slits widths $W_s > 20$ cm, a visual technique for measuring the observation length after the shot is as follows:

1. Locate the trajectory after the shot.

2. Place the eye on the trajectory viewing the mirror facet.

3. Move the eye along the trajectory and by observing the mirror facet, find the points on the trajectory where the slit first allows and then blocks transmission to the mirror facet.

These points give the trajectory length over which photons are collected. The uncertainty in estimating l_a by this visual method is estimated as about ± 2 cm. For setups with smaller slit widths (for example, $W_s < 10$ cm), the length over which the projectile is detected may be measured more accurately (than ± 2 cm) by placing a source on the trajectory, moving it along the trajectory, and measuring the response versus trajectory position with the IR system.

Both a PtSi array imager and a pyroelectric vidicon imager, the outputs of which are standard RS-170 video, were successful in recording projectile images. The PtSi imager has better spatial resolution, and therefore, its output was used to produce the temperature-calibrated M865 image shown later.

The PtSi imager responds from the transmission cutoff of its germanium lens at about 1.8 μm to the PtSi response cutoff at 5.5 μm. The pyroelectric imager responds from the cutoff of its germanium lens, also at 1.8 μm to beyond 14 μm. Each imager has considerable variations in spectral response within its nominal spectral pass band.

One shortcoming of the present setup is that since the rotating mirror is randomly oriented with regard to the projectile's location along the trajectory, it will not record the projectile if the mirror facet is oriented so that the reflected rays miss the imager lens. The system uses a 20-facet polygon with a PtSi imager. The imager lens has a diameter of 80 mm and a focal length of 100 mm. The imager's FOV is 7.2°. This imager used with the 20-facet polygon misses about half the shots. For most tests, both the PtSi imager and the pyroelectric imager were used simultaneously, each viewing a separate mirror facet on a single polygon. Usually, the projectile image was observed on one of the imagers.

The choice of a 20-facet polygonal mirror for the first system was a compromise based on several considerations. The polygon selection for a rotating mirror system involves a trade-off between the probability of detection and light gathering. Increasing the number of mirror facets for a given diameter and height polygon increases the probability that a facet will be oriented to reflect into the lens but reduces the facet's collecting aperture. Smaller facets require longer exposure times, which will increase image blur—an important consideration discussed in the next section. A rationale for selecting equipment must consider (a) projectile surface emissivity and temperature ranges to be detected, (b) placement of all optical components, (c) mirror to trajectory distance, (d) number of mirror facets, (e) possible image exposure from two facets (double exposure), (f) lens diameter, (g) imager FOV, (h) exposure time necessary to get workable signals with acceptable image blur, and (i) other factors. An analytical method for designing optimal rotating mirror systems for projectile imaging, which can select from among the many options, has not been found yet. One improvement over the present 20-facet polygon system would be to increase the number of mirror facets to 40, 50, or 60 etc., so that the image is always caught. The facet's collecting aperture would be smaller but it still might yield adequate signals when imaging projectiles under many conditions. For example, a smaller facet might still allow acceptable exposure times if the projectiles to be measured have high enough temperatures or if imager sensors with more responsivity were to be used (for example, InSb arrays).

2.1.1 *Blur Components*

For temperature measurements, the spatial resolution of the rotating mirror system limits the spatial features of the temperature distribution on the projectile surface, which can be measured. That is, for a radiating isothermal area to be assigned a temperature, its area must be somewhat larger than the area that is spatially resolved by the rotating mirror system. For example, if projectile surface areas many millimeters in extent are at nearly the same temperature, then resolution of a few millimeters will provide adequate imaging for thermal measurements.

When images of in-flight projectiles were first acquired, they appeared to have blurs and distortions, asymmetries etc., which showed considerable variation from shot to shot. In the sharpest images, the smallest spatial features that could be resolved on the projectile are estimated to be about 5 millimeters. However, most images did not show spatial features as small as 5 mm. The analysis that follows was completed after the images were acquired, in order to understand the sources of the image blurring. The analysis includes the effect of the exposure times on image blur. The most significant blurs are proportional to exposure time and can be reduced by simply shortening that time. For the in-flight images so far acquired, the exposure times were 200 to 300 μsec. The analysis has since shown that exposure times this long will cause considerable image blur. These exposure times could have been reduced since the video signal levels in most images were high.

When imaging with the rotating mirror system, several factors cause image blur of considerable magnitude. The individual blurs that have been identified are (a) velocity mismatch blur, caused by the error between the velocity of the imager's FOV and the velocity of the projectile, (b) misalignment blur, caused by an alignment error between the rotation axis of the mirror and the trajectory, (c) projectile spin blur, caused by projectile rotation during the exposure time, (d) defocus blur, caused by the error between the distance on which the system is focused and the actual distance to the trajectory, and (e) diffraction blur, caused by diffraction that usually occurs at the mirror facet but may also involve the edge of the lens if vignetting is present. Velocity mismatch blur, misalignment blur, and projectile spin blur occur because the image is not perfectly stable and translates during the exposure time. These blurs add vectorially. Defocus blur and diffraction blur are characteristics of the system's optics and do not change during the exposure time. Although these blurs have not yet been discussed, some idea of how the blurs combine in the image may be seen in Figure 9 which is discussed in Section 2.1.2.

For improving the quality of the image, the most effective approach is to identify the largest component blurs that can be reduced and begin by minimizing those blurs. Since some improvements in the image quality might be made by selection of equipment or choice of operating parameters, the sources of blur are described along with some approaches to improve the image quality.

The blur from each factor is estimated by considering how a radiating element on the projectile surface, a point source, is imaged throughout the exposure time. Since the amount of blur often depends on the source-to-image geometry, the blurs may vary somewhat, depending on where in the video frame the point source is recorded.

The blur components are all features of the image, in the so-called "image space" of the IR imager. One disadvantage of calculating blur in the image space is that the image is demagnified by the optics of each IR imager so that the actual blur dimension is imager dependent. Another disadvantage of giving the blur in dimensions of the image is that the demagnified blur dimensions still need to be translated into the projectile's dimensions because the main interest is seeing how small a spot on the projectile can be resolved. Both of these disadvantages can be avoided and the analysis is simpler and easier to visualize if the blurs are given in the corresponding dimensions of the projectile in the so-called "object space" of the projectile. Therefore, in the following analysis, whenever the blur is found in the dimensions of the image, it is then projected to the corresponding dimensions in the projectile's object space. When projected to object space, the blur is equal to $\Delta\theta \times R$, in which $\Delta\theta$ is the angle subtended (at the lens) by the blur in the image and R is the lens-to-projectile distance. Blurs that were first found in the image and then translated back to the object space are those caused by defocus and diffraction. When the image blur is caused by relative source motion during exposure, the source translation during exposure is used directly as the estimate for object space blur. These blurs include those from velocity mismatch, rotating mirror misalignment, and projectile spin. All final blur estimates are in dimensions of the projectile's object space.

2.1.1.1 Blur from Mismatch Between Projectile and Mirror Velocities

In the practical case, a velocity mismatch occurs between the projectile and the translation of the imager FOV. This mismatch occurs because values must be predicted before the shot and used in Eq.(2) to set the mirror speed and these predicted values are not exactly the same as those realized in the test. Specifically, the actual projectile velocity is different than that predicted, the actual mirror rotation rate differs slightly from the rate set before the shot, and the actual distance

actual distance between the trajectory and mirror, R_a, is different than the distance predicted before the shot, R_p.

The velocity mismatch (or velocity mismatch error), ΔV, is defined to be the difference between the velocity, V_a, of a radiating point source on the projectile surface and the linear motion of the imager's FOV at the distance, R_a, of the source,

$$\Delta V = V_a - 2\omega_a R_a. \tag{3}$$

The blur from velocity mismatch results from image motion in the direction along the trajectory and is proportional to exposure time,

$$B_v = \Delta V \Delta t. \tag{4}$$

A point source would appear in the image as a linear blur that corresponds, in dimensions of the projectile's object space, to a line B_v in length along the trajectory.

A. Velocity Mismatch for Short Ranges (< 0.5 km from gun)

The magnitude of the velocity mismatch can be estimated by considering how well the predicted values match the actual. Using V_p, R_p, and ω_p to represent values predicted before the test, the difference between the actual and predicted values are estimated in this section for systems placed close to the gun and in the next section for systems farther down range.

The component uncertainties for close ranges are

1) Projectile Velocity Projectiles that have completed the developmental phase and are ready for or in production [the so-called "type classified" projectiles] are estimated to have actual velocities, V_a, distributed within an interval of ± 1% of predicted velocity, V_p, with a level of confidence of 68%,[3]

$$V_a = V_p \pm \sigma_{V_a},$$

with

$$\sigma_{V_a} = 1\% \text{ or } 0.01\ V_p.$$

[3]In this report, uncertainty between two values is expressed by giving one value and an uncertainty interval and stating the probability of finding the second value within that uncertainty interval. An uncertainty interval of ± σ was chosen, in which σ represents a measured or estimated standard deviation. The second value is estimated to fall within the stated uncertainty interval of the first value with a level of confidence of 68%. See also Appendix D and Reference 15.

The predicted velocity is found from the published "firing tables" or may be measured from previous shots during the series of test shots.

2) Mirror Rotation Rate The uncertainty in the mirror rotation rate, that is, the difference between actual and set, is estimated to be $\pm$ 0.5% so that

$$\omega_a = \omega_p \pm \sigma_{\omega a},$$

with

$$\sigma_{\omega a} = 0.5\% \text{ or } 0.005\ \omega_p.$$

The accuracy of the mirror rotation rate appears to be one of the smaller sources of uncertainty.

3) Distance Between Trajectory and Rotating Mirror The trajectory is predicted to be a distance R_p from the imager, but the actual trajectory is R_a from the imager. For the case of an imager set up for large image size by placing it just a few meters off the trajectory, and for ranges within a few hundred meters of the gun, it is estimated that R_a will be within a few percent of R_p. There is apparently an uncertainty of a few tenths of a meter between R_a and R_p at close ranges, which is larger than predicted simply by the projectile's angular dispersion. The uncertainty probably results from a small systematic error in aiming and causes a bias of the center of impacts. In tests so far completed, only a small number of shots were fired and with so few shots, it is difficult to determine the true center of impacts and compensate for this bias with high accuracy. The accuracy that was achieved in experiments at ranges of 230 meters for several projectile types is estimated to be about $\pm$ 0.2 to 0.4 meter, or 3% to 7% of R when R = 6 meters. The uncertainty in R_a, for ranges of fewer than 500 meters, typical shot grouping, and with systems a few meters from the trajectory, is estimated as

$$R_a = R_p \pm \sigma_{Ra},$$

with

$$\sigma_{Ra} = 6\% \text{ or } 0.06\ R_p.$$

The uncertainty between R_a and R_p is probably the largest contributor to velocity mismatch blur when the following conditions apply: (a) for projectiles with highly predictable velocities, (b) for ranges of a few hundred meters, and (c) for setups where the rotating mirror system is placed a few meters off the trajectory to achieve large image size. These were the conditions for the tests so far completed. All tests occurred at a range of 230 meters from the gun.

The above estimates for uncertainties in V_a, ω_a, and R_a can be used with Eq. (3) to give statistical estimates of how much faster or slower the rotating mirror velocity will be relative to the projectile velocity. The component uncertainties propagate into the result, ΔV of Eq. (3), so that the probable resulting standard deviation (SD), $\sigma_{\Delta v}$, can be found by "root summing the squares" of the component uncertainties [15]:

$$\sigma_{\Delta V} = \sqrt{\left(\frac{\partial \Delta V}{\partial V_a}\right)^2 \sigma_{V_a}^2 + \left(\frac{\partial \Delta V}{\partial \omega_a}\right)^2 \sigma_{\omega_a}^2 + \left(\frac{\partial \Delta V}{\partial R_a}\right)^2 \sigma_{R_a}^2}\,.$$

Substituting for ΔV using Eq. (3), evaluating the partial derivatives and inserting gives

$$\frac{\partial\left(V_a - 2\omega_a R_a\right)}{\partial V_a} = 1, \quad \frac{\partial\left(V_a - 2\omega_a R_a\right)}{\partial \omega_a} = -2R_a, \quad \frac{\partial\left(V_a - 2\omega_a R_a\right)}{\partial R_a} = -2\omega_a,$$

$$\sigma_{\Delta V} = \sqrt{\sigma_{V_a}^2 + (-2R_a)^2 \sigma_{\omega_a}^2 + (-2\omega_a)^2 \sigma_{R_a}^2}\,.$$

Substituting the above estimated component uncertainties gives,

$$\sigma_{\Delta v} = 0.06\ V_p.$$

That is, with the estimated component uncertainties, the velocity of the rotating mirror's FOV will fall within 6% of the actual projectile velocity with a level of confidence of 68%. This uncertainty is simply dominated by the largest component, the 6% uncertainty in R_a.

To illustrate the velocity mismatch uncertainty in meters per second, a projectile velocity of 1500 m/sec is assumed and

$$\sigma_{\Delta v} = 0.06\ V_p,$$

$$\sigma_{\Delta v} = 90 \text{ m/sec}.$$

In this case, with a normal distribution, about 68% of the projectiles will have a velocity mismatch of 90 m/sec or less, 95% with 180 m/sec or less, etc.

The linear blur can be calculated using the velocity mismatch error and the exposure time in Eq. (4). The distribution of blurs follows from the distribution of velocity mismatches. For imaging projectiles with velocities under 2 km/sec by IR emission, exposure times in the range of tens to hundreds of microseconds are estimated as necessary to collect adequate signals.

This estimate is empirical and is based on the laboratory response test of the PtSi infrared imager, as described in Appendix B, and signal levels observed in many in-flight test recordings. Figure 3 indicates the magnitude of blur, B_v, for given velocity mismatches versus exposure time. The graph shows that it is important to minimize the exposure time, if possible to below 100 μsec, in order to reduce this blur component to a few millimeters.

B. Velocity Mismatch for Long Ranges (0.5 to 4.0 km from the gun)

While the tests so far completed have been done at relatively short ranges, long range measurements are also of interest. Therefore, a general analysis, relating to the probability of getting high resolution projectile images at ranges as far as 3 km, is also presented. To evaluate the magnitude of blur caused by velocity mismatch, the angular dispersion of the projectile trajectories is considered, along with the dispersion's effect on the error between R_a and R_p. The analysis gives velocity mismatch in terms of projectile dispersion and range.

When projectiles impact in a group and the center of impact is determined by the mean of each projectile's horizontal and vertical coordinates; the spread is usually described by the horizontal and vertical SDs of the shots from the center of impacts. The SD or dispersion in meters is then used to determine a subtended angle (from the gun) for that range and specified as the angular dispersion for the projectile. For example, if projectiles group with a horizontal linear dispersion of 0.8 meter at 2000 meters, then the horizontal angular dispersion is 0.4 milliradian at 2000 meters. For a normal distribution, 68% of the shot population will hit within plus or minus the dispersion, angular or linear, of the mean center of impact, 95% within two SDs, etc.

The horizontal linear dispersion is related to the angular dispersion and range,

$$\sigma_x = \sigma_\theta S,$$

in which σ_x is the linear dispersion, σ_θ is the angular dispersion at S, and S is distance from the gun to the range at which the dispersion is given.

Considering that the center of impacts has been found before or during testing and that the predicted hit point is used to predict the distance from the rotating mirror to the trajectory, R_p, the SD of actual R_a values from predicted R_p will equal the projectile's linear dispersion, σ_x,

$$R_a = R_p \pm \sigma_x,$$

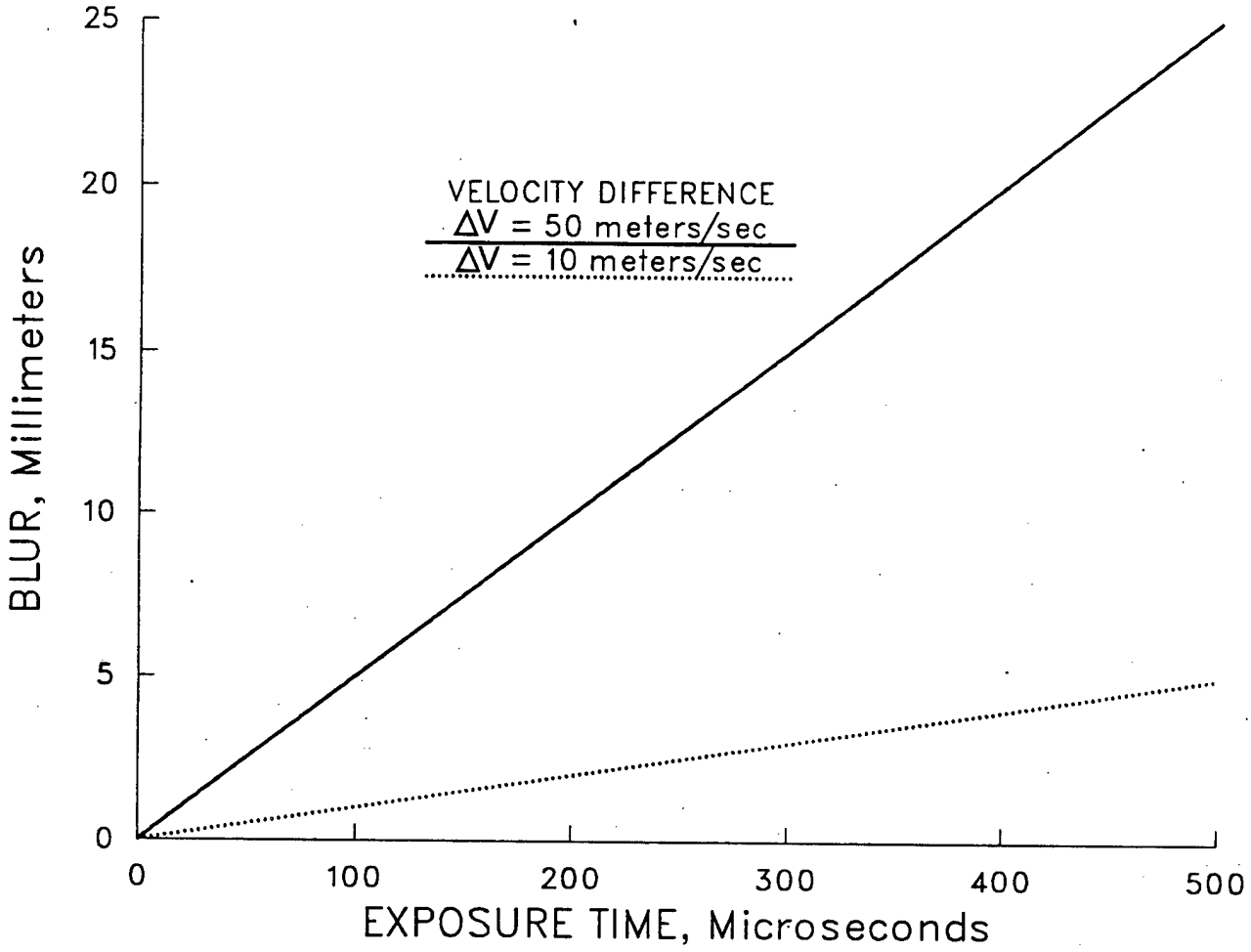

* A 3% error in R (R=6M) results in a mismatch of 50 m/s.

Figure 3. Blur From Velocity Mismatch Between Projectile Velocity and Rotating Mirror Velocity.

or in terms of angular dispersion, σ_θ,

$$R_a = R_p \pm \sigma_\theta S.$$

In general, the dispersion in the direction of R_p is needed. For these examples, it is assumed that the direction of R_p is horizontal and that σ_x and σ_θ are dispersions in the horizontal direction.

A special case is useful for seeing how the projectile dispersion limits the image quality by causing velocity mismatch blur. Consider that (a) the only source of mismatch is the difference between R_a and R_p which is described by the projectile's angular dispersion, (b) the actual and predicted projectile velocities are equal, and (c) the actual and set mirror rotation rates are also equal. Then the assumptions for this case are

$$R_a = R_p \pm \sigma_\theta S, \; V_a = V_p, \text{ and } \omega_a = \omega_p,$$

and when substituting these values into Eq. (3) and simplifying, the SD associated with the velocity mismatch is seen as

$$\sigma_{\Delta v} = 2\omega_p \sigma_\theta S. \tag{5}$$

Also, before the shot, the relation between the predicted values in Eq. (2) is used to find the desired mirror rotation rate ω_p

$$\omega_p = V_p/2R_p\,. \tag{6}$$

Substituting ω_p into Eq. (5), assuming no rotation rate or projectile velocity errors, gives $\sigma_{\Delta v}$ for the velocity mismatch in terms of the projectile's angular dispersion, σ_θ,

$$\sigma_{\Delta v} \; = \; \sigma_\theta S \, V_p/R_p. \tag{7}$$

If the velocity mismatch is dominated by the uncertainty in locating the trajectory because of the projectile's dispersion, that is, the rotating mirror is assumed to operate optimally, then Eq. (7) indicates the mismatch to be expected. Equation (7) indicates that the mismatch is inversely proportional to the distance away from the trajectory, R_p, with the implication that this blur can be indefinitely reduced by moving the rotating mirror away from the trajectory to increase R_p. However, Eq. (7) describes a special case and in the real case, as the mirror is moved back, at some point the rotation rate errors and uncertainty in the projectile velocity will make larger contributions to the velocity mismatch blur. (In addition, moving the system away from

the trajectory may cause the image size to become too small for acceptable spatial resolution with the IR imager.)

Rotating mirror instrumentation may have future application at down-range locations on firing ranges. The following example was chosen to illustrate the effects of projectile dispersion on velocity mismatch. Assume that the projectile has a velocity of 1500 m/sec and horizontal angular dispersions of 0.5 mrad at 1000 meters, 0.6 mrad at 2000 meters, and 0.8 mrad at 3000 meters. Assume that rotating mirror systems are situated at ranges of 1000, 2000, and 3000 meters and are placed 10 meters away from the trajectory as shown in Figure 4. Then estimated SDs for the velocity mismatch uncertainties for each mirror setup can be determined using Eq. (7) and are listed in Table 1.

Table 1

Velocity Mismatch Standard Deviation, $\sigma_{\Delta v}$, as a Result of Projectile Dispersion, σ_θ (with R_p = 10 meters)

S (meters)	σ_θ (mr)	$\sigma_{\Delta v}$ (m/sec)
1000	0.5	75
2000	0.6	180
3000	0.8	360

The distribution of blurs resulting from these mismatches can be estimated as a function of exposure time by considering the distribution of shots and referring to Figure 3. For a normal distribution with a mean velocity mismatch of zero, 68% of the shots will have a velocity mismatch within $\pm \sigma_{\Delta v}$, etc. The percent with velocity mismatch below any value of interest can be estimated from the distribution. For the example, the percent with velocity mismatch smaller than 50 m/sec is 50% at 1 km, 22% at 2 km, and 11% at 3 km.

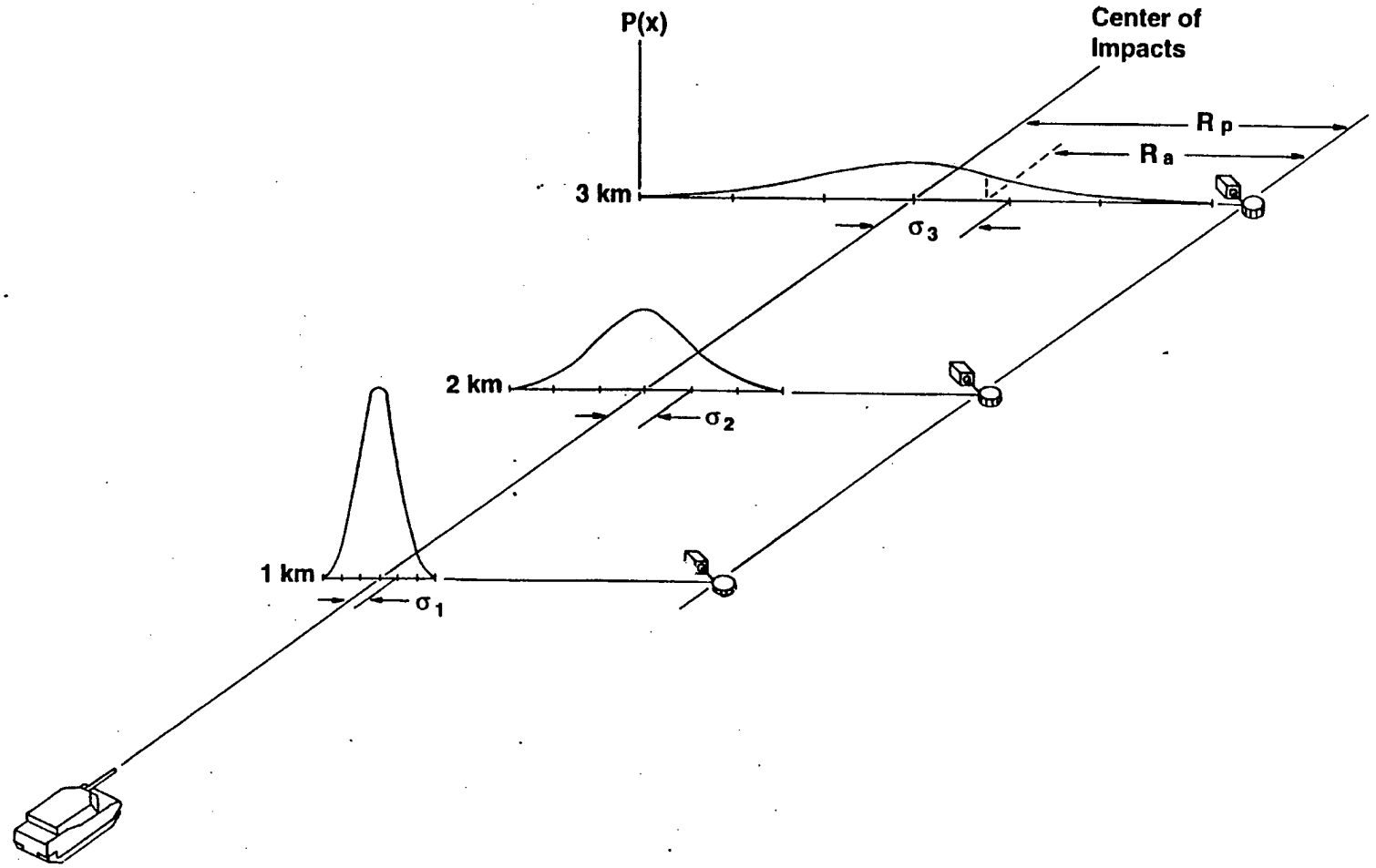

Figure 4. Down-Range Effect of Projectile Dispersion on Mirror-Trajectory Distance, R_a.

For long-range observations, two factors are important for the determining the velocity mismatch blur: the velocity mismatch itself and the exposure time. The velocity mismatch from the projectile's dispersion is one factor that is difficult to circumvent at long ranges. On the other hand, while the velocity mismatch increases with range, the final blur is also proportional to exposure time, a factor that will probably decrease with range. For projectiles that are observed down range after long aerodynamic heating times, higher surface temperatures will probably result and allow significant reductions in exposure time. The degree to which the increased velocity mismatch and reduced exposure time will offset one another with increasing range is highly dependent on the projectile's surface temperature.

To summarize, at long ranges, velocity mismatch blur will probably cause considerable blurring in many images, resulting in a reduced yield of useful data. The velocity mismatch is stochastic, however, and a portion of shots will have small velocity mismatch and yield sharp images. Therefore, if the yield of a few sharp images would be valuable and many projectiles are to be fired, then long-range experiments may still be worthwhile.

2.1.1.2 Blur from Alignment Error Between Mirror Rotation Axis and Trajectory

The axis of rotation of the polygonal mirror should be aligned in such a way that as the projectile moves, its image does not move in the direction transverse to the trajectory. To avoid image motion, the mirror's rotation axis should be normal to the plane containing the trajectory and the mirror facet center. The angle between the axis and plane normal, called the misalignment angle, is shown in Figure 5. If not so aligned, a blur occurs which is transverse to the trajectory.

If ϕ is the misalignment angle, then the alignment blur, B_a, in object space is

$$B_a = \sin \phi \, V_a \, \Delta t, \tag{8}$$

in which V_a is the projectile velocity.

The alignment blur can also be given in terms of the slit width, W_s,

$$B_a \approx \sin \phi \, W_s. \tag{9}$$

This simpler expression applies whenever slits are placed close to the trajectory so that the length over which a radiating element is observable is nearly equal to the slit width.

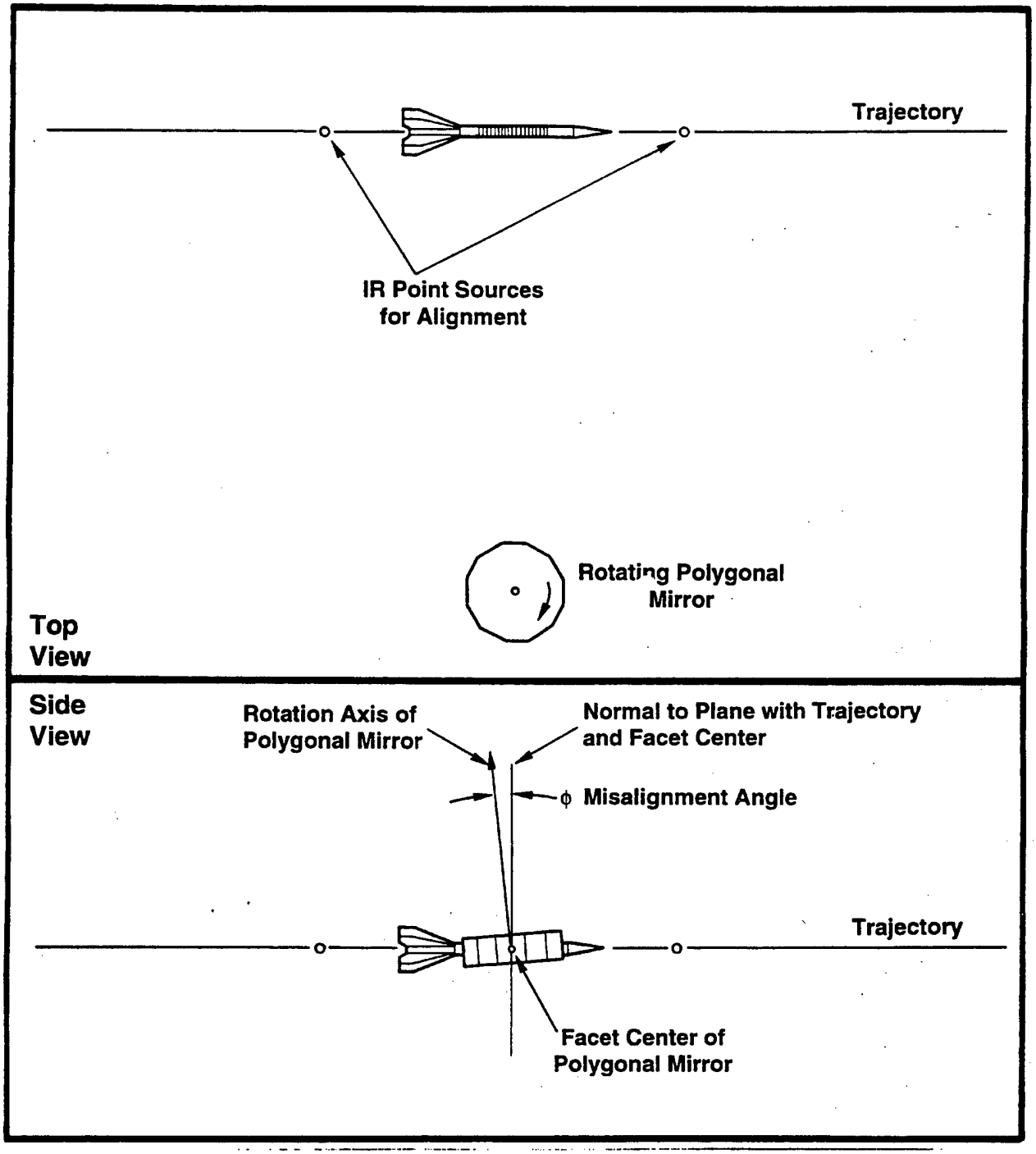

Figure 5. Alignment of Mirror Rotation Axis to Trajectory.

The alignment blur is transverse to the trajectory and is proportional to exposure time. The image translates with projectile motion in a direction predictable by the misalignment angle. It may, with a suitably accurate technique for aligning the mirror, be made negligible.

To illustrate the magnitude of the alignment blur for a typical example, with a 20-cm slit and mirror axis misalignment angle, ϕ, equal to 10 milliradians ($\approx 0.6^{\circ}$), the transverse blur would be

$$B_a = \sin \phi \, W_s,$$

with sin 10 mrad $\approx$ 0.01,

$$B_a = 2 \text{ mm}.$$

To align the mirror axis for the M865 tests, it was determined that the M865 trajectory was horizontal to within a few milliradians. A level was placed on the rotating mirror cover to align the mirror axis.

Since the M865 tests, an improved alignment technique was applied, employing two IR point sources placed near and parallel to the trajectory and mounted on a level as a reference. The placement of these sources is also shown in Figure 5. The alignment between the mirror axis and the trajectory can be conveniently observed by viewing the IR system's video monitor. When the mirror is rotating, the IR sources appear as two streaks across the video frame. When the mirror axis is tilted into alignment with the trajectory, the images of both sources fall on one line of detectors in the IR array as indicated by a single horizontal line on the video display. Considering the spacing of detector rows in the PtSi imager, the trajectory plane and rotating mirror axis are then aligned to better than 8 milliradians.

2.1.1.3 Blur from Projectile Spin

Many projectiles spin at high rates which, when imaged for the required exposure time, produce significant image blur. Among the projectile types, kinetic energy (KE) projectiles have the highest spin rates with values as great as a few hundred revolutions per second (rps). The exposure times needed for adequate video signals were estimated to be on the order of 100 microseconds.

The resulting blur is transverse to the trajectory. The blur is proportional to the distance between the radiating element and the projectile spin axis and therefore varies for different locations on the projectile. The blur also depends on the angular position of the radiating element relative to the system's viewing angle as described next. The blur at all image locations increases with the exposure time. Figure 6 shows the geometric features discussed next.

For a projectile with spin rate $d\Omega/dt$, the angular rotation, $\Delta\Omega$, during the exposure time, Δt, is

$$\Delta\Omega = d\Omega/dt\ \Delta t. \tag{10}$$

For example, if a projectile has a spin rate of 200 rps or $2\pi \cdot 200$ radians/sec and the exposure time is 100 μsec, then the projectile rotates 0.13 radian (7.2°) during exposure. Rotations of this magnitude will cause considerable image blur. The angular rotation, $\Delta\Omega$, for typical KE projectile spin rates of 100 and 200 rps are plotted versus exposure time in Figure 7.

The blur from spin for a radiating element on the projectile is given by

$$B_s = r \cos\alpha\ d\Omega/dt\ \Delta t, \tag{11}$$

in which r is the distance from the projectile spin axis to the radiating element and α is the angle between the line of sight from the imager to the spin axis and the line from the axis to the radiating element as shown in Figure 6 (the changes in α during the exposure time are assumed to be small).

To illustrate the magnitude of spin blur, a source point on a typical spinning KE projectile was chosen. The source point is located on a fin edge 5 cm from the projectile spin axis and is observed when the source is on the line of sight between the imager and spin axis, that is, with r = 5 cm, $\alpha = 0°$, and $\cos\alpha = 1$ as shown on Figure 6. These geometric conditions give the maximum blur since sources on other areas of the projectile surface, closer to the spin axis or with other α values, have less blur according to Eq. (11).

Figure 8 indicates the magnitude of spin blur, B_s in Eq. (11), for typical spin rates of 100 and 200 rps versus exposure time. Projectile spin causes considerable image blur for projectiles with higher spin rates when exposure times of about 100 μsec are needed for adequate signals.

An artifact may appear when rotating mirror imaging is applied to spinning projectiles and when the mirror axis is misaligned with the trajectory. The alignment blur may compensate for or add to the blur caused by spin. For example, if the spin moves the image of a fin edge down as it crosses the aperture slit but the alignment error moves its image up, these blur components would then tend to cancel. Since the spin blur varies with the location of the radiating element relative to the line of sight but the alignment blur affects the entire image equally, the net blur will vary across the image. An intentional misalignment might be introduced to compensate for

projectile spin over some areas of the image to improve, for example, the imaging of a fin edge on the line of sight.

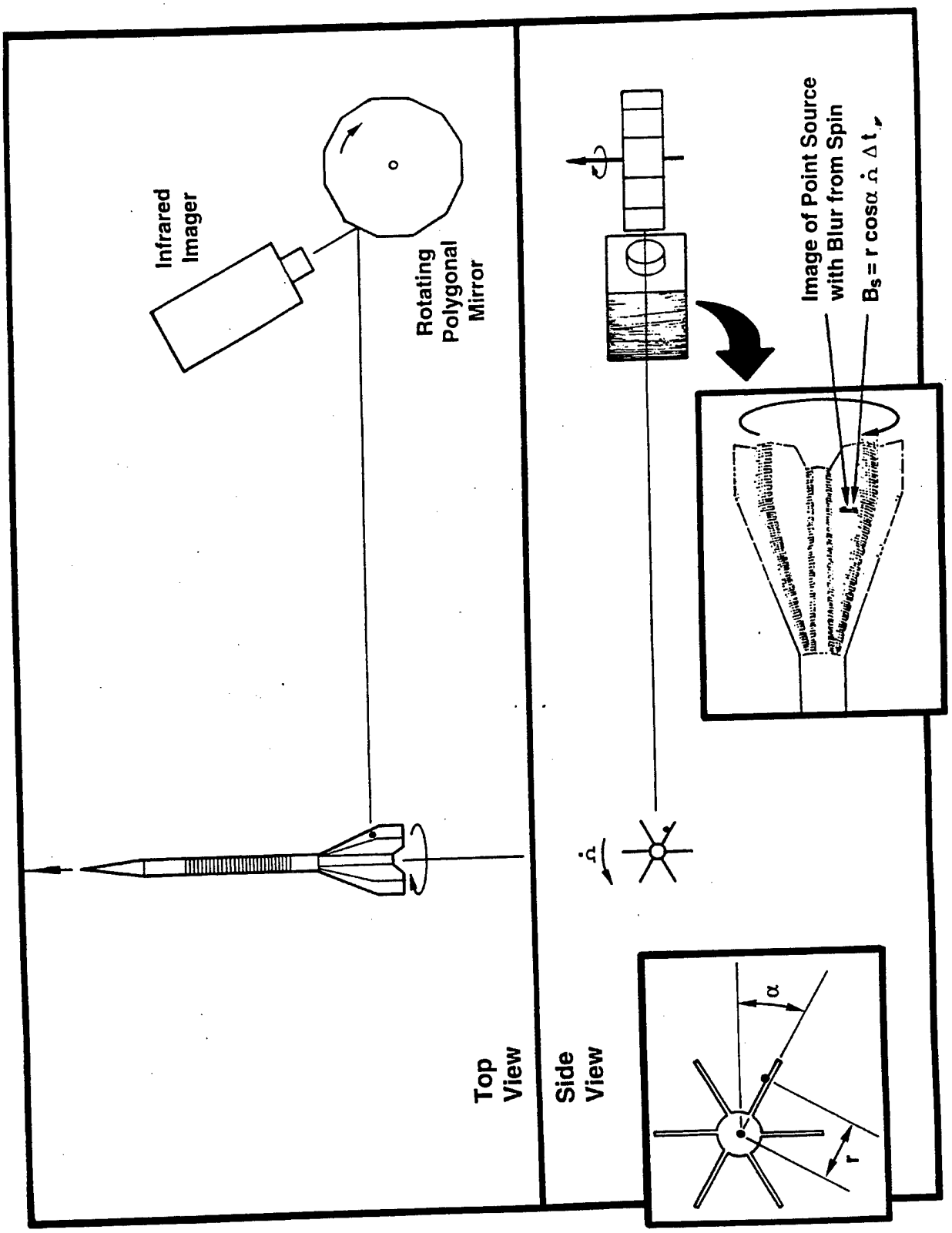

Figure 6. Spinning Projectile and Rotating Mirror Setup.

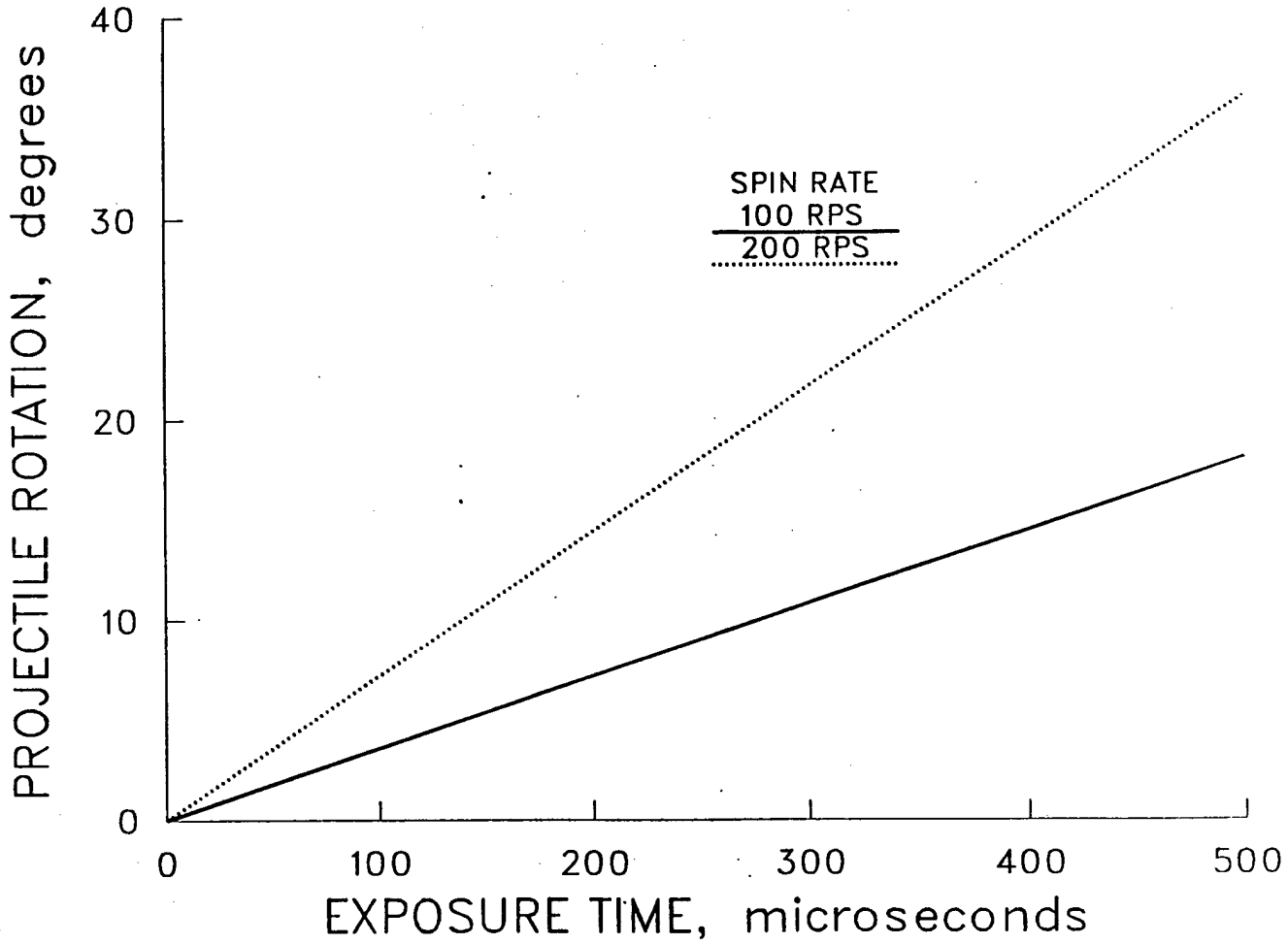

Figure 7. Projectile Rotation Versus Exposure Time.

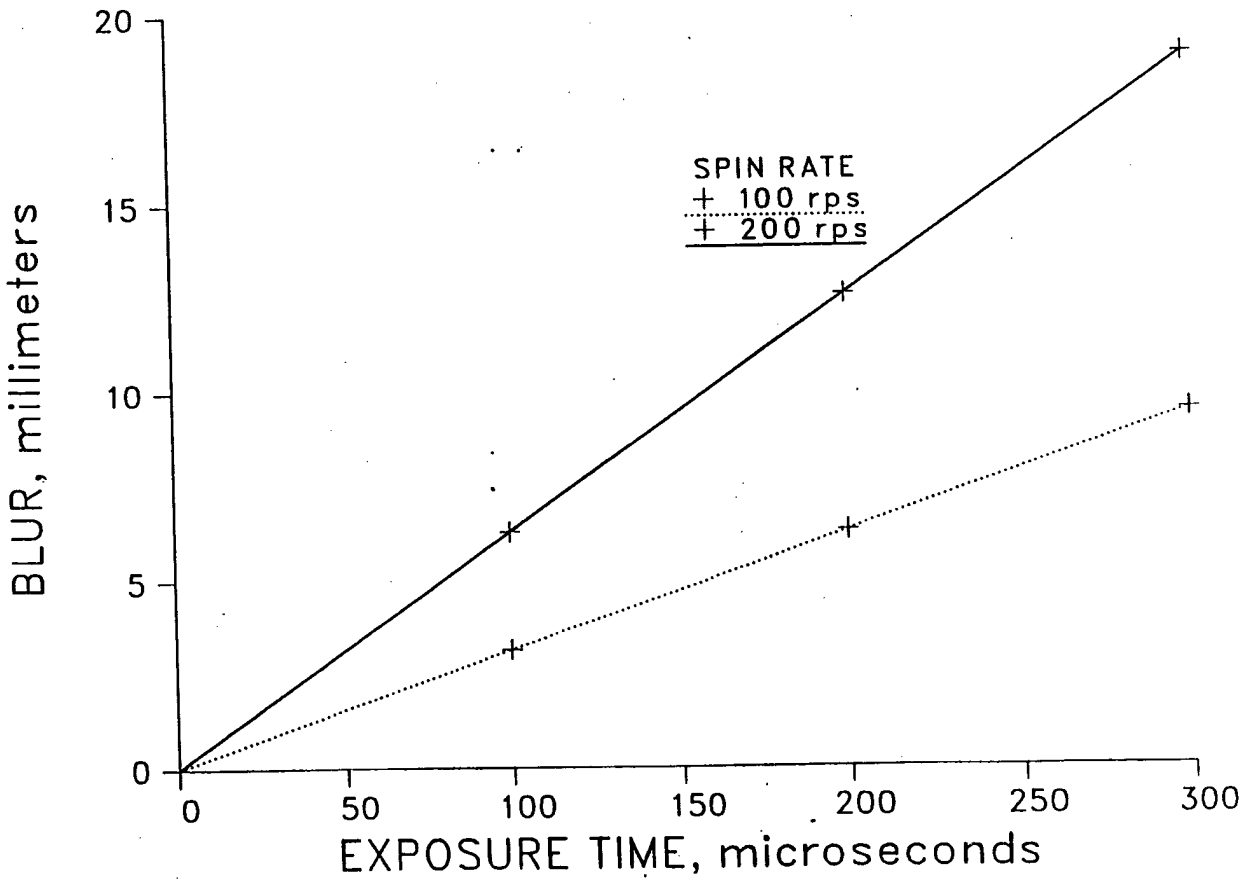

Figure 8. Example Blur From Projectile Spin Versus Exposure Time (for r = 50 mm and $\alpha = 0^{o}$, maximum blur for fin with radius of 50 mm).

2.1.1.4 Blur from Defocus

The trajectory, as discussed, will generally be displaced from that predicted before the shot. The imager is focused before the shot on the most likely distance to the trajectory, namely, at R_p from the mirror. The difference between the pre-shot focus distance and actual distance causes the image to be out of focus and adds a blur component.

The defocus blur in the rotating mirror is analogous to the "depth of field" blur for lenses with circular apertures. For the rotating mirror system, instead of the circular lens aperture, the limiting aperture is the facet that has width, W_f, and height, H_f. The blur and its corresponding object plane size are determined in a similar manner to that described for "depth of field" in Ref. 6.

The distance between the plane of best focus and the projectile is Z. For this application, $Z = R_a - R_p$, and assuming $Z << R_a$, a blur occurs in the image which subtends angle β,

$$\beta = \cos \psi \, W_f Z/R_a^2, \tag{12}$$

in which W_f is the width of the mirror facet and ψ is the angle of incidence for the IR bundle arriving at the facet. This angular blur is along the trajectory.

Likewise, for the angular blur transverse to the trajectory, the rotating mirror facet height, H_f, is used and the angle of incidence is equal to or less than one half the vertical FOV of the imager, a few degrees, so that $\cos \psi \approx 1$,

$$\beta = \cos \psi \, H_f \, Z/R_a^2.$$

The linear blur, B_f, along the trajectory in object space is the angular blur, β, multiplied by the distance to the object space,

$$B_f = \beta R_a,$$

$$B_f = \cos \psi \, W_f Z/R_a. \tag{13}$$

For example, using typical values from the M865 tests, if the mirror facet is 3 centimeters wide, the angle of incidence was 18°, and the imager was focused before the test at 6 meters and the actual trajectory was 5.7 meters away, then the blur along the trajectory using Eq. (13) would be

$$B_f = (0.95)(0.03\text{m})(6.0\text{-}5.7\text{m})/(6\text{m}),$$

$$B_f = 1.4 \text{ mm.}$$

For blur transverse to the trajectory, with facet height of 5 centimeters, the same degree of defocus, and assuming $\cos \psi \approx 1$,

$$B_f = (1)(0.05\text{m})(0.3\text{m})/(6\text{m}),$$

$$B_f = 2.5 \text{ mm.}$$

The defocus blur is (a) independent of the exposure time, (b) proportional to the facet width or height, (c) proportional to the distance between the actual trajectory and predicted plane of "best focus," and (d) inversely proportional to the distance from the imager lens to the trajectory.

In the section about blur from velocity mismatch, the relation between R_a and R_p was discussed in terms of the projectile's angular dispersion. The magnitude of blur from defocus will vary with R_a in the same stochastic manner as the blur from velocity mismatch.

The blur from defocus can be related to the projectile's angular dispersion. Assuming that the center of impacts has been found and that the imager is focused on the mean distance to the center of impacts, then the mean of Z will be 0 and the SD of Z values will be equal to the projectile's linear dispersion, $Z = 0 \pm \sigma_x$, or for angular dispersion, $Z = 0 \pm \sigma_\theta S$,

$$B_f = \cos \psi \, W_f Z/R_a,$$

$$B_f = \cos \psi \, W_f(\pm \sigma_\theta S)/R_a. \qquad (14)$$

For example, the defocus blur at 1000 meters for a projectile with angular dispersion of 0.5 milliradian, viewed by a mirror facet 3 centimeters wide which is placed 6 meters off the trajectory, is

$$B_f = 2.5 \text{ mm.}$$

The images will be degraded both by the blur from velocity mismatch and the blur from defocus. Both blurs have a similar dependence on the projectile's dispersion. To compare the blur from velocity mismatch to the blur from defocus, the ratio is formed of defocus blur given by Eq. (14) to velocity mismatch blur given by using Eq. (7) with Eq. (4), again assuming that the mirror is optimally operated as in the discussion of velocity mismatch,

$$\frac{B_f}{B_v} = \frac{\cos\psi W_f(\sigma_\theta S)/R_p}{\sigma_\theta S\, V_p/R_p\, \Delta t}, \tag{15}$$

assuming that cos ψ = 1,

$$\frac{B_f}{B_v} = \frac{W_f}{V_p \Delta t}. \tag{16}$$

When the projectile dispersion dominates the blur by making the location of the trajectory uncertain, then Eq. (16) indicates that the blur from velocity mismatch will equal the blur from defocus when the velocity times the exposure time equals the facet width. This obscure and difficult-to-remember relationship is useful for deciding how much can be gained by reducing the exposure time. Reducing the exposure time to reduce blur from velocity mismatch is only effective when that blur is larger than the blur from defocus. Further reduction of the exposure time to reduce blur will only cause the blur to approach the blur from defocus, which is independent of exposure time.

For example, with a mirror facet 3 centimeters wide and a projectile velocity of 1500 m/sec, the exposure time for these blurs to be equal, $B_v = B_f$, is

$$\Delta t = \frac{B_v W_f}{B_f V_p},$$

$$\Delta t = 20\ \mu\text{sec}.$$

In this case, as the exposure time is reduced below 20 μsec, the overall blur approaches the blur caused by defocus as a limit.

2.1.1.5 Blur from Diffraction

The spatial resolution will always be limited by diffraction [6]. This blur usually results from diffraction at the mirror facet but may also involve the lens aperture if vignetting is present. For most conditions, the blur from diffraction is smaller than the other described blurs. However, in cases when the other blurs are very small or for any system with narrow mirror facets, the diffraction blur may be considerable.

When a plane wave is diffracted by a rectangular aperture, like the mirror facet, and focused by a perfect lens, the central portion of the diffraction pattern, here used as the estimate for blur, subtends

$$\gamma = 2\lambda/W_f, \tag{17}$$

in which γ is the angular spread between the first minima on either side of the central maximum, λ is the wavelength, and W_f is the width of the facet, here considered the limiting aperture.

The corresponding dimensions in the projectile's object space are

$$B_d = \gamma R,$$

$$B_d = 2\lambda R/W_f . \tag{18}$$

For example, using Eq. (18), and choosing a midwavelength of $\lambda = 4$ μm, a facet width of 3 centimeters, and R = 6 meters, as in the M865 projectile tests, the blur is

$$B_d = 1.6 \text{ mm}.$$

2.1.1.6 Imager Array Spatial Resolution

The blurs discussed so far pertain to the image presented to the IR array. In addition, the resolution limits of the IR detector array are likely to further limit the video image realized. For example, on the PtSi array, the dimensions of the elemental detector are 23 μm in the horizontal direction and 32 μm in the vertical direction. Imaging from 6 meters off the trajectory with a 100-mm focal length lens, the FOV of each detector in the projectile object space, estimated here by geometric optics, is about 1.4 mm horizontally and 1.9 mm vertically.

The estimate of the detector's horizontal FOV can be compared to the system's diffraction limit, estimated before, to see if the detector size or the diffraction is most limiting in the video image. The detector's geometric FOV is 1.4 mm, and the diffraction limit for 4 μm photons is slightly larger at 1.6 mm. This FOV is reasonably matched to the diffraction limit. For rotating mirror applications, the other identified blurs will almost always be larger and therefore will determine the image quality.

2.1.1.7 Image Noise from Microphonics Caused by the Projectile Shock Wave

In addition, for tests with systems placed close to the trajectory, the shock wave from the projectile causes a considerable portion of the images to be degraded with microphonic noise. If the shock wave reaches the IR imager or recorder before the video image has been read from the detector array and recorded, all or some of the video lines will be degraded. The effect has produced noise in the recorded video signals with magnitude as great as 20% of full video level. When these video images are displayed, the noise also causes jitter in triggering of the horizontal sweep, which distorts the image by shifting the individual horizontal lines. The higher frequency

components have durations of a few hundred microseconds, which exceed the horizontal sweep time and cause characteristic lines across the entire frame width. The M865 image presented later has been slightly degraded by this noise.

This noise can be avoided by moving the system away from the trajectory so that the video image is always recorded before the shock wave reaches the system's vulnerable component. The recording will be completed if the travel time of the shock wave - from the trajectory to imager or recorder at the speed of sound - is less than the total time it takes the system to acquire and record the image. For example, if an imager detects, has a negligible delay for video processing, and outputs at frame rates of 30 frames/sec with 33 milliseconds between frames, the system will always detect and complete the recording before the shock wave hits, if placed 11 meters or more away from the trajectory. For the in-flight projectile experiments, all of which took place inside the Transonic Range of the U.S. Army Research Laboratory, shock wave microphonic noise was present in most of the video images. This noise could not be avoided by moving the equipment away from the trajectory because the outer wall of the firing range building restricted the placement of equipment to a maximum of 6 meters away from the trajectory. Another approach would be to attenuate the shock wave by placing the imager and recorder in a protective box.

2.1.2 *Composite Blur*

The described blur components combine in the image. Figure 9 gives a generic composite image showing how a point source on the projectile might be imaged onto the IR array. The directions in the image plane that are parallel and transverse to the projectile's trajectory are shown. The diffraction blur or "limit," usually smaller than the defocus blur, is shown for reference. The defocus blur and diffraction blur are independent of exposure time. The blurs from velocity mismatch, projectile spin, and mirror misalignment add vectorially to cause image motion. These image motion blurs are proportional to exposure time. As mentioned, the spin blur varies, depending on location of the source point on the projectile. In a given setup, image motion from projectile spin and mirror misalignment may be in opposite directions and tend to cancel.

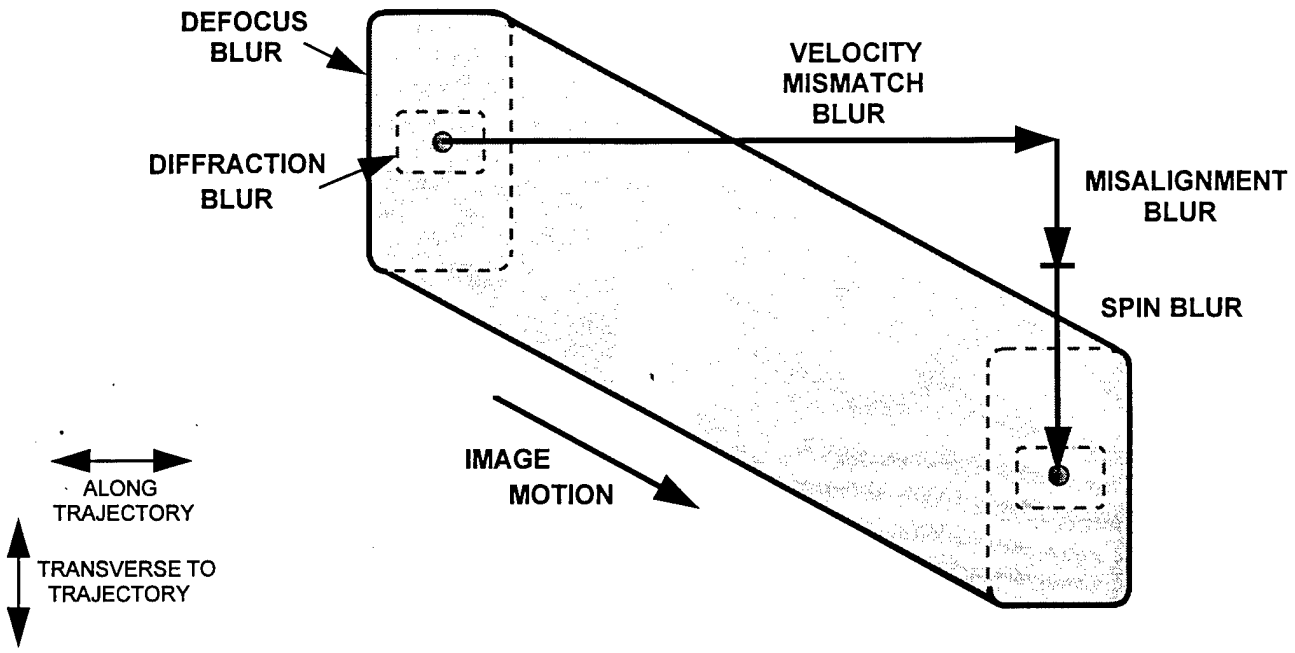

Figure 9. Composite Blur Showing How the Five Blurs Combine in the Image Plane to Degrade the Image of a Point Source on the Projectile's Surface.

2.2 Calibration of the Rotating Mirror System for In-Flight Projectile Temperature Measurements

The objective in video thermography is to measure the temperature of a thermal source by acquiring an IR image and calibrating the video levels to show temperature. In most applications, the thermal source and the IR imager are stationary. In the thermography of in-flight projectiles, however, there is a very high relative velocity between the source and imager. In most other regards, the thermography of in-flight projectiles is analogous to the thermography of stationary thermal sources, which is well covered in the literature [7]. For some years, in closely related experiments, IR imagers have been used to measure temperatures on stationary aerodynamic models in wind tunnels [8-10].

This section gives the background and rationale for the temperature calibration of in-flight projectile images. The spectral band of the temperature measurement is an important consideration in calibration, and therefore, this section starts with a brief discussion of the spectral features of both the radiating projectile and the rotating mirror system. Next, the radiometric equation that relates the system's video output to the temperature on the projectile's surface is derived. A calibration procedure is described in which a heated model of the projectile and a blackbody simulator (BBS) are used in combination to simulate the in-flight projectile recording. The radiometric relationships between the in-flight projectile, projectile model, and

BBS are shown. Last, the calibration procedure that was used to measure a M865 training projectile is described as an example.

In-flight projectiles have heated surfaces that emit photons across a broad spectrum. The directional and spectral emissivities of projectile surfaces are not completely known. Some projectile surfaces have industrial finishes, such as thick oxide layers, which have predictable emissivities. For example, aluminum alloys are often anodized with a layer of Al_2O_3, from 50 to 120 μm thick, which is known as "hard coat." This surface is characterized in the literature as having a high emissivity (about 0.9) with little dependence on direction or wavelength (high emissivity graybody). In general, however, projectiles will have at least some component surfaces with unknown emissivities. The temperature calibration technique, described later, accounts for the emissivities of projectile surfaces by measurements made on a heated laboratory model of the projectile.

The rotating mirror system operates over a broad spectral band. The system detects photons from across as broad a spectral band as practical in order to reach adequate signal levels with minimum exposure times. The blur analysis has shown that the shortest possible exposure time is desirable for reducing image blur since most of the blur components are proportional to the exposure time.

The emitted photons are transmitted through the system with some spectral absorption and finally reaching the detector, the photons are converted, also with a wavelength dependence, to signal electrons. The complete rotating mirror system includes the IR imager, polygonal mirror, any other optical components, and the air path. The system's spectral response is known to a considerable degree, but not completely, from the spectral response curves of the sensor and spectral transmission curves for the optical components and air path. Generic curves or those supplied by the manufacturers give the approximate values. For example, the generic response curve for a PtSi Schottky-barrier detector indicates that the long wavelength cutoff is at about 5.5 μm. The spectral transmission of the imager's germanium lens determines the short wavelength cutoff of the system, about 1.8 μm because of bulk germanium absorption. Between 1.8 and 5.5 μm, the PtSi imager has considerable variation in spectral response because of the combined effects of the spectral transmission of the lens coating and spectral response of the PtSi detector. The assembled rotating mirror system also includes the polygonal mirror and any additional optical components. The spectral transmissions of these components also contribute to the system's overall spectral transmission. The system's overall spectral transmission is therefore usually not completely known in broadband applications.

In summary, the projectile source and rotating mirror system together have spectral characteristics that are broadband and known to some degree but not completely. Next, the video signals produced in these broadband measurements are discussed.

The video image of an in-flight projectile is comprised of many individual signals generated in the individual detectors of the PtSi array. The signal in any individual detector is produced by the thermal radiation of a corresponding small area on the projectile surface. By the nature of thermal radiation (a strong dependence of radiance on temperature [7]), the detector's signal also shows a strong dependence on the temperature of the projectile's surface. The video signal is measured (in millivolts or relative units) from the recorded image of the in-flight projectile. The objective is (once the video signal is measured) to assign a temperature to the corresponding source area on the projectile's surface. Temperatures can be assigned once the signal versus temperature (S_d vs T) for the in-flight recording is known. In this case, the S_d vs T for the in-flight projectile recording is calibrated using reference sources at known temperatures.

The basic radiometric relationships between a thermal radiator's temperature and radiance and the detector's video signal are given in the literature [7,13]. Reference 7 has a useful general treatment for continuous sources in which the relevant equations are Eos.(4-54), (4-221), and (4-36). The following derivation reaches similar expressions by another method. In addition, the derivation describes systems that collect for a brief integration time, as the PtSi video imager does when it captures the in-flight projectile. The symbols and terms as defined in the following derivation correspond, in most part, to those in Ref. 7.

The following derivation gives the radiometric relationship between the projectile source and the output signal of a single detector on the imager's array. The signal discussed in the derivation is that produced by the source after any contribution from background has been subtracted. Also, linearity has been assumed between the irradiance on the detector and the system's output signal. For clarity, at the beginning of the derivation, only monochromatic radiation is treated and the system is considered to have no absorption losses. Later, the wavelength-dependent properties and absorption are included.

This derivation follows simply from the definition of radiance. The radiance of a thermal radiator indicates the radiant flux, in watts or photons per second, which is emitted per unit projected area of source per unit solid angle. For a source of radiance, L, and projected area, A, the total flux, Φ, collected by a system with solid angle, G, focused by the lens, and received by a detector on the array is equal to

$$\Phi = A\ G\ L,$$

in which A is the projected area at the source that fills the detector's FOV, as determined by geometric optics. (The unit area, as defined for radiance, is the "projected area," the normal of which lies in the direction of the observation.) The solid angle, G, for the rotating mirror system, is that subtended (at the projectile source) by the mirror facet or, if vignetting is present, subtended by the mirror-lens combination (solid angle issues are discussed in detail in a later section).

As used, the video imager produces a single image when the projectile passes. In this case, the flux is collected during a brief exposure time, Δt, and the resulting energy ($\Delta t \times \Phi$) is converted into electrons with some quantum efficiency usually given in electrons/photon. Later, the accumulated electrons are read from the array as charge packets, amplified with some gain, and processed into the video signal. The ratio between the video output and the irradiating energy is given as the detector's responsivity, $\Re$, in millivolts/joule. The video signal, S_d, which represents the energy collected during the exposure time with $\Re$ serving as a proportionality constant, is given by

$$S_d = \Re\ \Delta t\ \Phi,$$

or, in terms of radiance by substituting for Φ,

$$S_d = \Re\ \Delta t\ A\ G\ L.$$

So far, only monochromatic radiation has been considered. However, the radiance, L, and responsivity, $\Re$, are both wavelength dependent and, therefore, the solution for the total signal is an integration over wavelength. Also, the system has been considered to be without absorption losses. Some flux is absorbed in the air path and components of the system and will not reach the detector. The system's transmission is also wavelength dependent and is given by the spectral transmission, $\tau(\lambda)$.

The detector signal then, recognizing the wavelength dependencies and absorption by inserting $\Re(\lambda)$, $L(\lambda)$, and $\tau(\lambda)$, and integrating, is

$$S_d = \Delta t G A \int_0^\infty \Re(\lambda)\tau(\lambda)L(\lambda)d\lambda.$$

In addition, the radiance, L, of a real surface is customarily described as the product the surface's emissivity, ε, and the fundamental blackbody radiance, $L_b(\lambda,T)$, in which T is the temperature of the real surface. The emissivity varies with wavelength, direction and temperature, and is given by $\varepsilon(\lambda,\theta,\phi,T)$.

Finally, the emissivity, $\varepsilon(\lambda,\theta,\phi,T)$, and blackbody spectral radiance, $L_b(\lambda,T)$, can be substituted for L, to give the general equation for the signal produced in an array detector by a thermal radiator such as a small area on the projectile's surface

$$S_d(T) = \Delta t G A \int_0^\infty \Re(\lambda)\tau(\lambda)\varepsilon(\lambda,\theta,\phi,T)L_b(\lambda,T)d\lambda . \tag{19}$$

The objective is to obtain S_d vs T, which calibrates the video image and allows it to display temperature. Eq. (19) could, in principle, be used to calculate the system's signal as a function of temperature. However, the equation's components that have spectral dependencies, $\Re(\lambda)$, $\tau(\lambda)$, and $\varepsilon(\lambda)$, are not adequately known in broadband applications, and therefore, the integral is unsolvable, as discussed in Reference 11. The S_d vs T is then determined empirically by a calibration procedure.

This next part gives a description of the calibration. It begins with a brief description of the calibration steps in the sequence in which they were performed. First, the signal produced by the in-flight projectile was recorded. After the in-flight projectile was recorded, a BBS was used to calibrate the system's response in the field. The BBS simulated the input to the system produced by the in-flight projectile by using similar conditions of exposure time, system collection solid angle, etc. In a separate laboratory calibration measurement, the system responses to the BBS and to a heated model of the projectile were compared. The comparison was used to complete the temperature calibration of the in-flight projectile image.

To describe the radiometric relationships among the three sources (in-flight projectile, laboratory projectile model, and BBS), the general integral, Eq. (19), is used repeatedly with the subscripted quantities identifying different sources, setups, etc. Inserting the subscripted quantities that apply to the in-flight projectile test into Eq. (19), the detector signal for the in-flight recording is

$$S_d(T_a) = \Delta t_a \overline{G}_a A \int_0^\infty \Re(\lambda)\tau_a(\lambda)\varepsilon_a(\lambda,\theta,\phi,T_a)L_b(\lambda,T_a)d\lambda, \tag{20}$$

in which

Δt_a - system exposure time

$\overline{G}_a$ - system's average collection solid angle during the exposure time

A - projected area of the radiating projectile component that fills the detector's FOV

$\Re(\lambda)$ - detector spectral responsivity

$\tau_a(\lambda)$ - system spectral transmission

$\varepsilon_a(\lambda,\theta,\phi,T_a)$ - spectral directional emissivity of the in-flight projectile component in the direction $[\theta,\phi]$ to the system

T_a - temperature of the in-flight projectile component

$L_b(\lambda,T_a)$ - spectral radiance of a blackbody at component's temperature, T_a

After the image of an in-flight projectile has been recorded, the system's S_d vs T_a is calibrated by simulating all the quantities that are in Eq. (20).

In describing the calibration, the rationale is simpler to follow conceptually if the laboratory model is considered to have been used instead of the BBS (which was actually used) in the field calibration. The use of the BBS as a substitute for the laboratory model is separately explained. For now, let us imagine that the laboratory projectile model itself, instead of the BBS, is to be used for the field calibration.

The emissivities of the in-flight projectile components are simulated by the laboratory model. The model is simply a projectile that comes from the same manufacturing lot as the in-flight projectiles fired in testing. The projectile is shortened to fit in a small oven. The emissivity of the model then closely simulates the emissivity (spectral, directional, and thermal dependence) of the in-flight projectile. For the in-flight projectile recording, the directional emissivity causes the signal from a component to depend on the viewing angle and therefore, that same viewing angle is used for calibration with the laboratory model component. If the component of the in-flight projectile has experienced launch or flight damage, which significantly changes its emissivity, this approach of using the laboratory model may not be useful.

The emissivity of a component on the laboratory projectile model is

$$\varepsilon_s(\lambda,\theta,\phi,T_c),$$

in which T_c is the temperature of the component. Because the laboratory projectile comes from the same manufacturing lot as the in-flight projectile, it is assumed that its emissivity, at the same temperature as the in-flight projectile, $T_c = T_a$, is equal to that of the in-flight projectile,

$$\varepsilon_s(\lambda,\theta,\phi,T_c) = \varepsilon_a(\lambda,\theta,\phi,T_a).$$

Also, the spectral radiance versus temperature for each component surface on the model is then the same as the spectral radiance versus temperature for the corresponding component on the in-flight projectile. (It is assumed that IR reflections make a negligible contribution to the radiance.) Then, the spectral radiance of the laboratory model and in-flight projectile are also equal whenever $T_c = T_a$,

$$\varepsilon_s(\lambda,\theta,\phi,T_c)\, L_b(\lambda,T_c) = \varepsilon_a(\lambda,\theta,\phi,T_a)\, L_b(\lambda,T_a). \tag{21}$$

The laboratory model may then be used to simulate the spectral radiance versus temperature of the in-flight projectile over a range of temperatures when the temperature of the laboratory model is controlled and known.

In addition to the projectile's spectral radiance, the other quantities in Eq. (20) are also simulated in the field calibration of the rotating mirror system. The system calibration is done *in situ* after recording the in-flight projectile without changing the components, their locations or the imager's electronic settings. The exposure time, Δt_a, is first estimated by the technique already described and then simulated as time, Δt_s, by using a chopper between the reference source and system. The average solid angle, $\overline{G}_a$, is simulated by a fixed solid angle, G_s. A detailed discussion of the average solid angle and the simulated solid angle is in the next section. The source area, A, remains unchanged for the in-flight projectile and field calibration since the image-object geometry is reproduced by placing the reference source directly on the trajectory. The detector's spectral responsivity, $\Re(\lambda)$ remains unchanged since the imager's electronic settings (gain and offset, etc.) were not changed. The in-flight transmission, $\tau_a(\lambda)$, is simulated as $\tau_s(\lambda)$ in the field calibration by using the same air path length and optical components.

Using Eq. (21) for the spectral radiance and substituting the other simulated quantities in Eq. (20), the equation that describes the laboratory model as set up to simulate the in-flight recording is

$$S_d(T_c) = \Delta t_s G_s A \int_0^\infty \Re(\lambda)\tau_s(\lambda)\varepsilon_s(\lambda,\theta,\phi,T_c)L_b(\lambda,T_c)d\lambda. \tag{22}$$

S_d vs T_c in Eq. (22) of the simulation is the same as S_d vs T_a in Eq. (20) for the in-flight recording to within the accuracy of the simulation. The experimental uncertainties between the simulated and in-flight quantities, Δt_s and Δt_a, ε_s and ε_a, etc., and the resulting experimental uncertainty in the simulation are discussed in Appendix D. S_d vs T_c can be found empirically by

viewing the model of the projectile and increasing its known temperature in increments. The in-flight recording would then also be calibrated for temperature.

The laboratory projectile as an IR reference source heated to known temperature is the standard on which the temperature calibration is based. The laboratory model could conceivably be used directly for post-shot field calibration by heating it to known temperature, controlling its output pulse with a chopper, and observing it with the rotating mirror system (in which case, this explanation of the rationale for calibration would be much simpler and now complete).

However, the model's temperature is difficult to control in the field and the model would require a large chopper. Therefore, in the actual field calibration of the rotating mirror setup, a BBS served as a substitute for the laboratory model. The method of calibrating that uses the BBS as a "transfer" reference is now described.

The system's responses to the BBS and to the laboratory model were compared in laboratory measurements. The signal produced by the laboratory model is

$$S_d(T_c) = \Delta t_l G_l A \int_0^\infty \Re(\lambda)\tau_l(\lambda)\varepsilon_s(\lambda,\theta,\phi,T_c)L_b(\lambda,T_c)d\lambda, \tag{23}$$

in which the subscript l indicates tests in the laboratory.

The signal produced by the BBS, also in the laboratory, is

$$S_d(T_b) = \Delta t_l G_l A \int_0^\infty \Re(\lambda)\tau_l(\lambda)\varepsilon L_b(\lambda,T_b)\, d\lambda, \tag{24}$$

in which for a BBS, ε is nearly 1. For comparison, the exposure times, solid collection angles, and detector's FOV were kept equal for the BBS and projectile model by direct substitution of the BBS for the model. Then $\Delta t_l G_l A$ is the same for Eq. (23) and Eq. (24).

To compare the sources, the laboratory model was first heated in an oven to temperature, T_c, viewed by the system, and the system response, $S_d(T_c)$, measured. The laboratory model was then replaced by the BBS in the optical setup. The BBS's temperature, T_b, was then adjusted until it produced the same system response, that is, $S_d(T_c) = S_d(T_b)$. Optical and electronic conditions for the system were unchanged. The temperature of the laboratory model was increased in steps and the measurements repeated. Over a wide temperature range, the pairs

of T_c and T_b that produce equal system response were recorded and plotted in a curve. Figure 10 gives the T_c vs T_b curve for the M865 projectile test. (The M865 component shown, the "tail flare," has a high emissivity anodized aluminum surface so that its output nearly equals that of the BBS.)

When the signals from the BBS and laboratory model are equal, that is,

$$S_d(T_c) = S_d(T_b).$$

then the integral sides of Eq. (23) and Eq. (24) are also equal,

$$\Delta t_1 G_1 A \int_0^\infty \Re(\lambda)\tau_1(\lambda)\varepsilon_s(\lambda,\theta,\phi,T_c)L_b(\lambda,T_c)\,d\lambda = \Delta t_1 G_1 A \int_0^\infty \Re(\lambda)\tau_1(\lambda)\,L_b(\lambda,T_b)\,d\lambda. \quad (25)$$

Then for the T_c and T_b pairs shown in the calibration curve, the wavelength-dependent parts of Eq. (25) are equal,

$$\int_0^\infty \Re(\lambda)\tau_1(\lambda)\varepsilon_s(\lambda,\theta,\phi,T_c)L_b(\lambda,T_c)\,d\lambda = \int_0^\infty \Re(\lambda)\tau_1(\lambda)\,L_b(\lambda,T_b)\,d\lambda. \quad (26)$$

However, while the integrated system responses are equal, the spectral distribution of photons arriving on the detector from the projectile model is not generally the same as the spectral distribution of photons from the BBS. Note. While a BBS was used in these tests as the transfer source, use of the known absolute radiance of the BBS is not necessary in the calibration procedure. Also, other broadband IR sources with reproducible outputs in the system's response band would work as well as the BBS.

In order to use the laboratory results in the field, the system transmissions for the laboratory and field must be considered. The overall system transmission, τ, is determined by the combined transmissions of the optical components and the air path. In the M865 projectile test, the same optical components were used in both the field and laboratory. The air path length for the field setup was 6 meters and for the laboratory setup, 3 meters. The broadband transmission of a 6-meter air path is nearly equal to that of a 3-meter air path. Therefore, the overall laboratory and field transmissions are nearly equal, $\tau_l(\lambda) \approx \tau_s(\lambda)$, and $\tau_s(\lambda)$ may be substituted for $\tau_l(\lambda)$ in Eq. (26),

$$\int_0^\infty \Re(\lambda)\tau_s(\lambda)\varepsilon_s(\lambda,\theta,\phi,T_c)L_b(\lambda,T_c)\,d\lambda = \int_0^\infty \Re(\lambda)\tau_s(\lambda)\,L_b(\lambda,T_b)\,d\lambda. \quad (27)$$

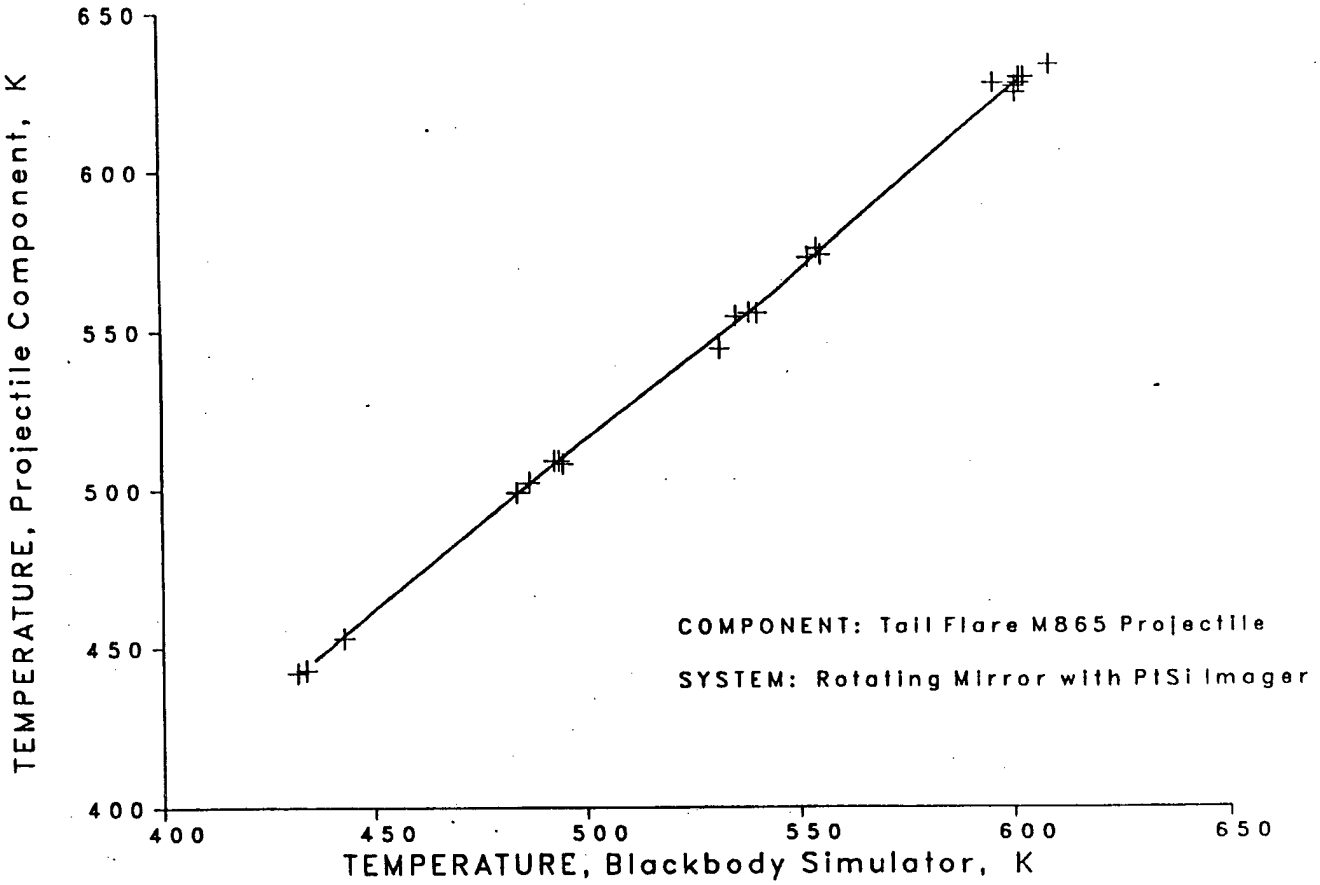

Figure 10. Projectile Component Temperature Versus Blackbody Simulator Temperature for Equal Response From Rotating Mirror System (laboratory calibration using model projectile and BBS).

This equation shows the temperatures at which the BBS and projectile oven model would produce the same system response in the field.

In the actual field calibration, the BBS was used to produce a system S_d vs T_b curve in which

$$S_d(T_b) = \Delta t_s G_s A \int_0^\infty \Re(\lambda)\tau_s(\lambda)L_b(\lambda, T_b)\, d\lambda. \tag{28}$$

The same system output, according to Eq. (27), would also have been produced by the laboratory model at T_c. Using Eq. (27) to substitute for the BBS in Eq. (28),

$$S_d(T_c) = \Delta t_s G_s A \int_0^\infty \Re(\lambda)\tau_s(\lambda)\varepsilon_s(\lambda,\theta,\phi,\ T_c)L_b(\lambda, T_c)\, d\lambda. \tag{29}$$

Eq. (29) is seen to be the same as the simulation equation, Eq. (22). As mentioned, the S_d vs T_c of Eq. (22) is the same as the S_d vs T_a of Eq. (20) for the in-flight projectile. Therefore, either the BBS or the laboratory model can be used to produce the S_d vs T_c, which simulates the S_d vs T_a of the in-flight projectile. In practice, the S_d vs T_b curve is measured and is transformed into the S_d vs T_c curve by simply replacing T_b by the T_c shown on the laboratory curve.

The use of the BBS as a transfer reference for the laboratory oven model (in which T_a always equals T_c, and T_c is related to T_b by the temperature values given in the laboratory curve) can be summarized in the following block diagram:

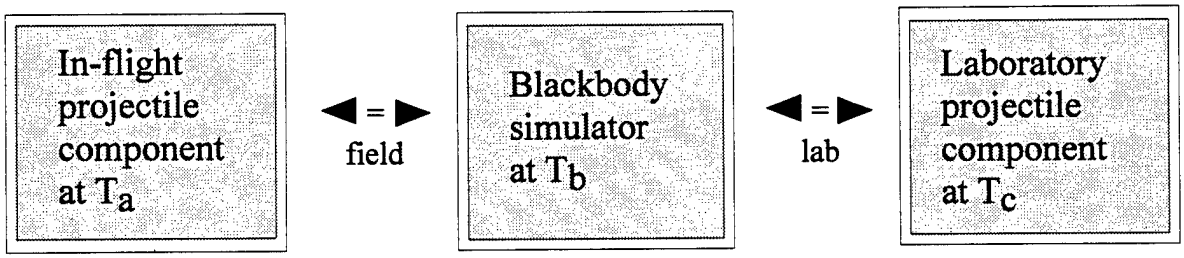

2.2.1 *System Collection Solid Angle During In-Flight Recording*

The signal developed by the rotating mirror system depends on the collection solid angle, G, which varies from shot to shot and during the exposure time so that it requires consideration in the calibration. At the time the projectile enters the slit opening and becomes detectable, the mirror is oriented with some angle and rotates to follow the projectile as it moves. Since the

position and continued motion of the projectile and the orientation and continued rotation of the mirror affect the system's geometric configuration, the solid angle of the system, which is collecting photons, may be different from shot to shot and during each recording. The system's solid angle may be limited, or vignetted, if some of the facet reflection hits the lens edge and is blocked, as shown in Figure 2. The initial lens blockage when the projectile first appears behind the slit is most important; the subsequent changes in solid angle during recording are much less important. The solid angle does not change significantly during a single recording because the mirror typically rotates less than 2°, which results in a total translation of the facet reflection across the lens of only a few millimeters. The total translation in the setup for the M865 test was 6.8 mm, shown as "**A**" in Figure 2, and is small in comparison to the width of the facet reflection (30 mm).

The following three geometric factors influence the system's collection solid angle and must be considered in calibration:

1. Vignetting of the mirror reflection by the lens aperture may occur: (a) there may be no vignetting and all of the facet reflection may pass through the lens throughout the entire exposure time; (b) the vignetting may vary somewhat during the exposure time because as the facet reflection translates slightly across the lens, it may be blocked by more or less of the lens aperture as illustrated by "**A**" in Figure 2; or (c) the facet reflection may entirely miss the lens and not produce an image, which of course will not require further calibration.

2. Vignetting also occurs briefly between the slit and mirror facet. The slit edges control the exposure time by blocking the path between the projectile and mirror facet. As the projectile travels along the trajectory, initially the first slit edge blocks photons from reaching the mirror facet, then photons are transmitted to the facet to begin the exposure time and finally, the second slit edge blocks once again to end the exposure time. The important rays are shown emanating from the slit edges in Figure 1. While during most of the exposure time the full facet receives light, there is also a partial blocking of the facet just as the projectile is entering or leaving the measurement region of the trajectory, that is, just as the shadow from the respective slit sweeps across the mirror facet. This partial blocking is analyzed by taking rays from an elemental source area on the projectile surface and tracing those rays as the projectile travels. Considering a point source on the projectile as it first arrives, the time it takes for these "shadow" rays to go from fully blocking the mirror facet to no obscuration, Δt_o, is

$$\Delta t_o = \frac{D_{ts} W_f \cos \psi}{V_a (R_a - D_{ts})},$$

in which D_{ts} = trajectory-to-slit distance, W_f = facet width, ψ = angle of incidence onto facet, V_a = projectile velocity, and R_a = distance from the trajectory to the rotating mirror.

For typical values of D_{ts}, W_f, R_a, etc., from the M865 test setup, some of which are shown in Figure 1, Δt_o = 3 μsec. The time required for the projectile to both enter and leave, the total obscuration time, is 6 μsec.

To see if the obscuration time is considerable, it can be compared to the exposure time. The exposure time for this test was about 300 μsec. In this case, partial blocking occurred during 6 μsec or 2% of the exposure time of 300 μsec. Partial blocking for such a small fraction of the exposure time, if ignored in the calibration procedure, will cause a negligible error in temperature measurement. This error is estimated to be approximately 1 K. If, however, the obscuration time becomes a considerable fraction of the exposure time, for example, when the narrowest slits are used to minimize the exposure time, this effect is no longer negligible and needs attention in the calibration procedure.

3. As the mirror rotates, the projected collecting area of the facet changes. For rotations of a few degrees or less, the projected area is nearly constant and this consideration is negligible.

2.2.2 *Post-Shot Technique to Evaluate Collection Solid Angle*

As the projectile moves along the trajectory, the rotating mirror ideally maintains a reflecting angle throughout recording so that the IR photons emitted by a point on the projectile always reach a single image point as recorded. The angular relationships for the rays are shown in Figures 1 and 2. The known relationship between the source position, rotating mirror angle, and recorded image position can be used after the shot to closely reproduce the geometric configuration that existed when the projectile source was located at any trajectory point. Reproducing the geometric configuration will reproduce the solid angle used for collection and allows relative system response to be measured for any trajectory point. The entire trajectory observable through the slit can be examined point by point. The measured relative responses primarily indicate the degree of vignetting for the trajectory points.

To take advantage of this relationship, a source is placed at a sample coordinate point along the trajectory. The mirror is manually rotated so that the image of the source falls on the region of the imager's frame in which the in-flight projectile component was recorded. The rotating mirror's configuration therefore becomes identical to that existing when the in-flight projectile source was located at that trajectory point during the recording of the in-flight image. The system's relative response can then be measured for each trajectory point. The electronic settings (imager gain and offset, etc.) and optical setup, except for the mirror rotation angle, are kept the same for both the recording of the in-flight projectile and the post-shot field calibration procedure. The relative responses of several sampled points can be averaged to give an average response for a projectile traveling across the slit or to determine that as the projectile moved the relative response did not vary significantly in terms of causing temperature errors. This latter case is probably true for most recordings because the few millimeters of translation caused by mirror rotation of 2° or less will usually have a small effect on vignetting at the lens aperture.

The relationships between the in-flight average solid angle, the simulated solid angle used in calibration, and the solid angles and system responses for the points along the trajectory, which are used to evaluate the accuracy of the simulation, are described next.

The signal from the in-flight projectile is given by Eq. (20),

$$S_d(T_a) = \Delta t_a \overline{G}_a A \int_0^\infty \Re(\lambda)\tau_a(\lambda)\varepsilon_a(\lambda,\theta,\phi,\ T_a)L_b(\lambda,T_a)\ d\lambda.$$

As discussed, to calibrate Eq. (20), the BBS is placed at a reference location, x_r, with solid angle, $G_s(x_r)$, and its temperature increased in increments to give the field calibration curve, S_d vs T_b. Equation (28) gives the signal from the BBS as used in the field calibration,

$$S_d(T_b) = \Delta t_s G_s(x_r) A \int_0^\infty \Re(\lambda)\tau_s(\lambda)L_b(\lambda,T_b)\ d\lambda.$$

The accuracy of the simulation depends on how closely $G_s(x_r)$ in Eq. (28) simulates the average in-flight solid angle, $\overline{G}_a$, in Eq. (20). A technique for evaluating $\overline{G}_a$ and comparing it to $G_s(x_r)$ is now described.

The in-flight solid angle averaged across the projectile's travel can be represented by an average of the solid angles for n points along the trajectory, in which x_i is the coordinate for each point,

$$\overline{G}_a = \frac{\sum_{i=1}^{i=n} G_a(x_i)}{n}.$$

The solid angle for any trajectory point used in the in-flight recording can be reproduced after the shot by the technique just described. Then, for the same trajectory points, the actual and post-shot solid angles are equal,

$$G_s(x_i) = G_a(x_i),$$

$G_s(x_i)$ may be substituted for $G_a(x_i)$ in the sum for $\overline{G}_a$,

$$\overline{G}_a = \frac{\sum_{i=1}^{i=n} G_s(x_i)}{n}.$$

According to Eq. (22), the system's measured responses, $S_d(x_i)$, are proportional to the solid angles, $G_s(x_i)$, when other system conditions (Δt_s, T_b, etc., in Eq. [22]) remain unchanged as in the field calibration procedure,

$$G_s(x_i) = K \times S_d(x_i),$$

and the system responses may be substituted for the solid angles in the sum,

$$\overline{G}_a = \frac{\sum_{i=1}^{i=n} K \times S_d(x_i)}{n}.$$

Finally, to determine how well $G_s(x_r)$ simulates the average in-flight $\overline{G}_a$ the ratio of the signals can be used

$$\frac{\overline{G}_a}{G_s(x_r)} = \frac{\dfrac{\sum_{i=1}^{i=n} K \times S_d(x_i)}{n}}{K \times S_d(x_r)}, \qquad (30)$$

$$\frac{\overline{G}_a}{G_s(x_r)} = \frac{\dfrac{\sum_{i=1}^{i=n} S_d(x_i)}{n}}{S_d(x_r)}.$$

If the ratio is near unity, then $G_s(x_r)$ is a close simulation of $\overline{G}_a$. In the M865 test, for example, $\overline{G}_a$ was about 98% of G_s, as calculated by the ratio of signals as shown in Appendix C. If the ratio is not near unity, a correction may be applied.

2.2.3 *Example Procedure Used for Field Calibration in the M865 Projectile Tests*

To illustrate the calibration procedure, the M865 projectile test is described. First, the steps are briefly summarized: (a) the in-flight projectile was recorded, (b) the system response to a BBS reference source was determined at a reference location on the trajectory, (c) the relative response for other trajectory points seen through the slit were measured, and (d) a comparison was made between the BBS and laboratory source and used to temperature calibrate the in-flight image of the M865 projectile.

Next, a more detailed description of the M865 calibration is given as follows:

1. Record Test Data The M865 projectile image was recorded within a range of video levels, which is suitable for calibration, given the imager's dynamic range. For example, the PtSi imager produces video output, which is a useful indicator of temperature change from about 10% to 90% of video saturation.

The only component resulting in a useful image was the conical tail "flare" on the M865 projectile (shown later in Figure 12).

2. Locate Reference Source on Trajectory After the shot, the trajectory was located and the BBS reference source was placed on the trajectory at a selected reference location. The slit center, marked "0 cm" in Figure 1, was used as the reference location, x_r, in the M865 tests. As discussed in Section 2.2.2, the mirror was rotated so that the image of the BBS fell on the same frame location on which the M865 tail flare was recorded.

3. Set Blackbody Simulator Pulse Timing

Pulse Duration: The BBS chopper was operated so that the pulse duration matched the exposure time of the in-flight test measurement. The pulse duration was set to equal the time that a source element on the projectile radiates to the rotating mirror. In the M865 test, the actual exposure time was about 300 μsec (see description of rotating mirror system for how to determine exposure time). The chopper was operated for simulated exposure time of 250 μsec, and a small correction was applied to the measured signal level because the simulated exposure time was about 17% less than the actual.

Pulse Repetition: The BBS shutter was operated to output one pulse every several seconds to simulate test conditions regarding exposure of the imager's sensor, that is, a long time with only background infrared then a brief single exposure from the in-flight projectile.

4. Record Video Level Versus BBS Temperature (S_d vs T_b) The full range of video levels to be calibrated in the image of the in-flight projectile component was determined. The BBS was set to a temperature that produced a smaller video level than the lowest to be calibrated in the image of the M865 tail flare and many video images of the pulsed BBS were recorded. The temperature was increased in steps, and images of the BBS were recorded at each temperature. The temperature was increased until both the highest video level in the recorded M865 image and system's video saturation level were included.

At this point, a system calibration for video level versus BBS temperature, S_d vs T_b, was complete for the selected reference location, the slit center. Figure 11 is a graph of S_d vs T_b. Next, the relative responses of the other trajectory points were measured by applying the technique described in the previous section.

5. Measure Relative Response Versus Trajectory Location To determine the relative responses for points along the trajectory to the response of the reference location (slit center), the BBS, at a single temperature that produced mid-level video respons., was moved to locations along the trajectory, and the rotating mirror was manually rotated so that the image of the BBS fell on the same frame location as the in-flight projectile component. The geometric configuration of the rotating mirror system was then identical to that existing when the projectile source was located at that trajectory point during the recording of the in-flight test image. System responses to BBS pulses at sampled trajectory points across the slit were recorded. The relative responses versus trajectory location were determined by comparing video levels from the sampled trajectory points to the video level measured when the BBS was located in the slit center.

The projectile radiated to the system along about 48 cm of the trajectory. The four trajectory locations at which relative responses were measured covered only about 34 of the 48 cm. For post-shot analysis of the data, two additional trajectory locations would have supplied a more complete characterization of the collection solid angle along the trajectory. However, for additional projectile travel along the trajectory, projectile translations of 7 cm correspond to facet reflection translations across the lens of only 1 mm. The lens aperture is 80 mm in diameter and the cross section of the facet reflection is about 30 x 50 mm. Therefore, a facet translation of only 1 mm will not cause the solid angle to change very much from those at the four other trajectory points that were measured. The translation for the entire exposure time is shown as "**A**" in Figure 2.

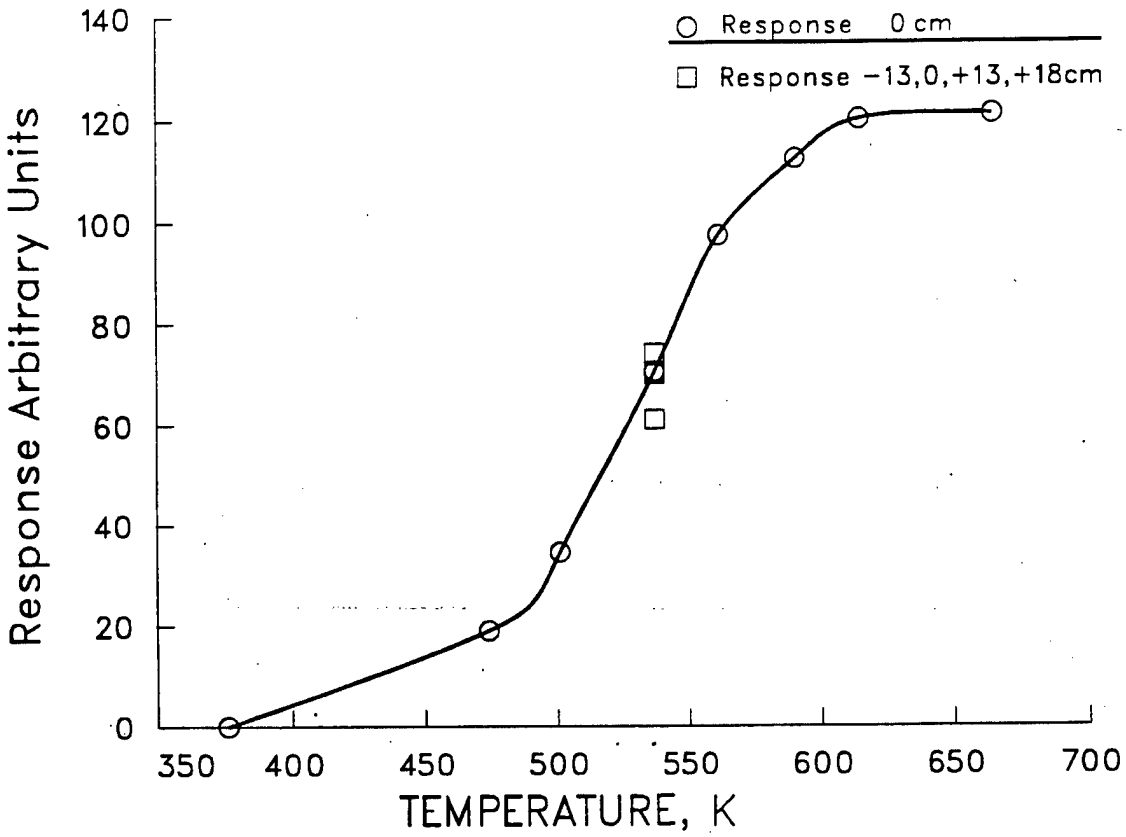

Figure 11. Rotating Mirror System Response Versus Pulsed Blackbody Simulator Temperature . (The curve indicates the response for a temperature scan of the BBS placed at the slit center, 0 cm. Responses are also indicated for the BBS at a fixed temperature of 537 K placed at -13, +13, and 18 cm.)

The missing data for the M865 test are handled by increasing the estimate of experimental uncertainty and are discussed in Appendix D.

For the M865 test, the video levels were sampled at 0 cm (slit center) and at -13, +13, and +18 cm from the center. (The missing data would have been taken with the source placed at about -20 and +22 cm.) The scale used to locate the points is shown on Figure 1. At each location, the system response to four BBS pulses was measured and appears in Appendix C. The mean responses at the three locations indicated video levels -13%, +5%, and -1%, respectively, from the mean video level at the center of the slit. The mean responses are also plotted on Figure 11. The average response for the four locations was 98% of the mean response measured for the slit center. Because the average response did not vary significantly from that at the center, the S_d vs T_b calibration of Figure 11 for the slit center was used without modification as representative of the average response to a source moving along the trajectory behind the slit. In the M865 test, the mirror rotated less than 2^o and the facet reflection translated a total of 6.8 mm across the lens aperture as the projectile passed. This translation did not change the system's collection solid angle very much as was indicated by the measured responses.

The uncertainty in knowing and simulating the in-flight projectile's radiometric quantities for calibrating the video level results in an uncertainty in the measured temperature. The system's reproducibility was estimated from the data observed in Appendix C, and the uncertainties associated with the components of the simulation (exposure time, collection solid angle, radiance, etc.) were estimated in Appendix D. The resulting uncertainty between the signal produced by the in-flight projectile and the signal produced by the post-shot simulation is ± 21% of the signal level as estimated in Appendix D. The experimental uncertainty in temperature associated with a ± 21% radiometric uncertainty (in the mid-range of video levels in Figure 11) is about ± 15 K. In addition, an uncertainty of ± 16 K is presently assigned to cover possible bias in the oven model temperature which serves as reference for the calibration procedures. The experimental uncertainty in temperature measurement in the M865 test is estimated in Appendix D as ± 22 K. This experimental uncertainty applies to the mid-range video levels, which are discussed later in Section 3.1 and are indicated by the color red in Figure 12.

In-Flight Measurement Reproducibility

Presently, too few measurements are available for statistical analysis of the reproducibility of the signal levels produced by similar in-flight projectiles. However, two additional M865 projectiles were recorded with very similar video levels, and some comments about these recordings follow.

A second image of a M865 tail flare was captured in the same frame location as the calibrated image. It had microphonic noise, which degraded the image shape, and was not further processed. The video levels in this image of the tail flare are generally 20% lower than those of the M865 image presented later in Figure 12. The observed signal difference of -20% results from the combined effects of measurement reproducibility and real temperature differences on the M865 tail flares between the shots. If the measurement were perfectly reproducible and all the difference were the result of real temperature differences between the shots, then the 20% lower signal could result from a temperature difference of only about -15 K (estimating from the field calibration curve, Figure 11). A third M865 image with similar video levels was realized, but it cannot be directly compared because it was situated in a different area of the frame that was not calibrated.

3. RESULTS

3.1 M865 Projectile Image with Temperature Calibration

The temperature-calibrated image of the in-flight M865 projectile appears in Figure 12. The projectile's tracer was removed before firing. The projectile velocity was about 1610 m/sec. The image was captured at a range of 230 meters from the gun, at which point, the projectile was about 0.14 second into its flight. The heating then results from the gun launch process and 0.14 second of aerodynamic heating.

The projectile's conical tail "flare" was detected. The base of the flare is 77 mm in diameter and it has a wall thickness of 7 mm. Toward the base of the flare are notches with dimensions of 13x20 mm. One notch is imaged and its shape is resolved despite some slight degradation of the image by the microphonic noise from the projectile's shock wave, as discussed. The body itself did not radiate above the image's background level and the nose was not imaged within the FOV. The color red was assigned to display surface temperatures in the range of 500 to 550 K. The color white indicates roughly 600 K or greater. The range of video levels assigned red covers about 25% to 70% of the full range of video levels as shown in Figure 11. The experimental uncertainty for all video levels within the red band is estimated in Appendix D at about ± 22 K with a 68% level of confidence. The uncertainty in the white areas, not estimated, is larger because the video levels are approaching saturation. The second object, which is imaged as a white line forward of the tail flare on the body of the projectile, is a ring of rubber sealant used to seal the sabot segments to the M865 body. Combustion may be present on this rubber ring.

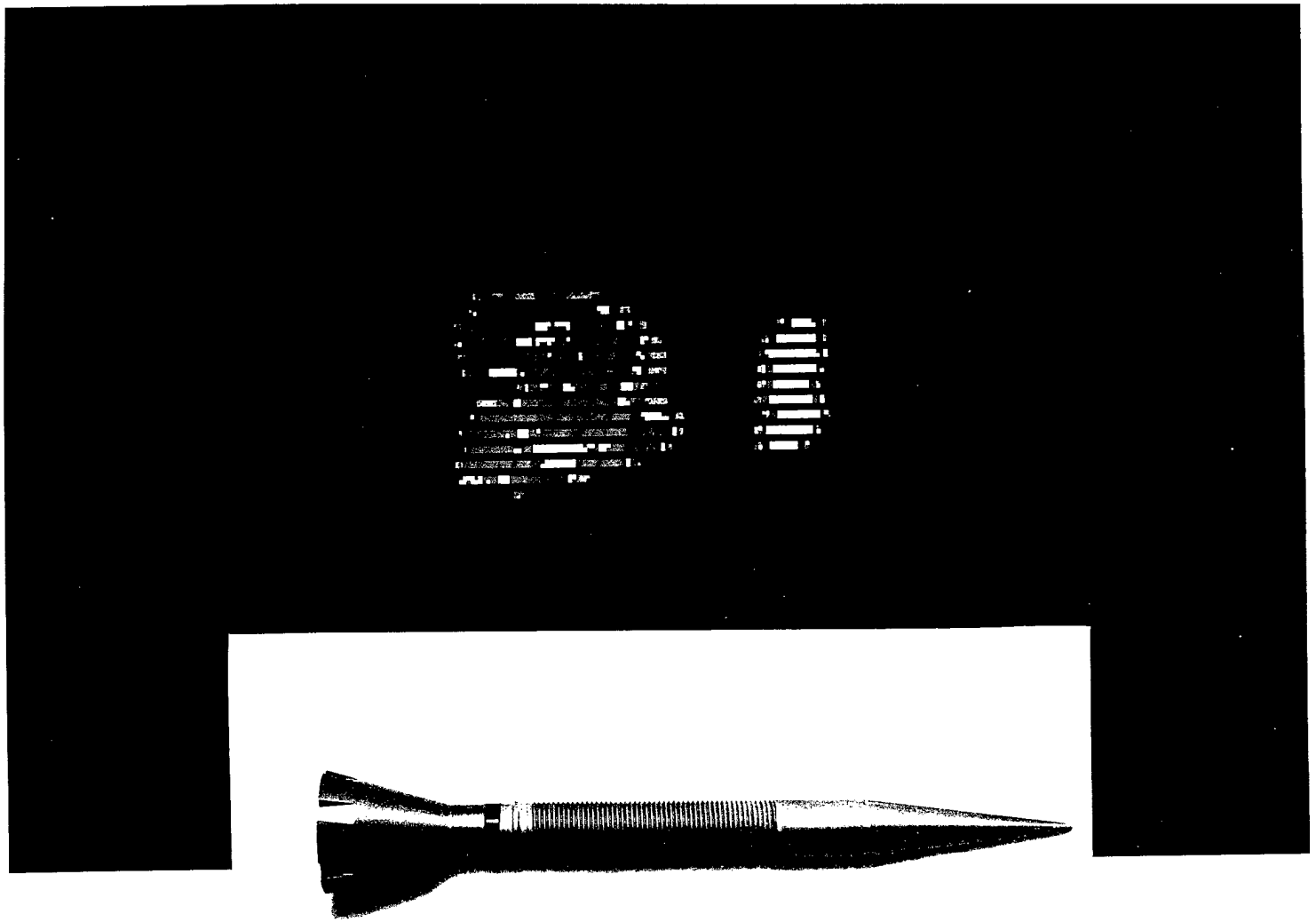

Figure 12. Temperature-Calibrated Image of In-Flight M865 Projectile. (Red is assigned to surface temperatures in the range of 500 to 550 K.)

Since the molecular by-products of combustion may receive non-thermal excitation and emit radiation that cannot be used for thermography, no temperature is assigned to this ring.

4. CONCLUSIONS

A rotating mirror was applied to acquire IR emission images of in-flight high velocity projectiles. The characteristics of the system that affect image quality were analyzed and methods of reducing blur described. The analysis can be applied to determine the likely yield of both useful and high quality projectile images for future down-range instrumentation. A technique was developed to calibrate the IR video images for temperature. The surface temperature distribution of an M865 in-flight projectile was measured and displayed.

INTENTIONALLY LEFT BLANK

5. REFERENCES

1. Bundy, M.L., Horst, A.W., and Robbins, F.W., "Effects of In-bore Heating on Projectiles" BRL-TR-3106, U.S. Army Ballistic Research Laboratory, Aberdeen Proving Ground, Maryland, June 1990. (AD B145805)

2. Weinacht, P., Sturek, W.B., Wooden, P., "Computational Study of Inbore and In-flight Heating for 105mm, M774 Projectile Modified Swept Fin" ARBRL-MR-03377, U.S. Army Ballistic Research Laboratory, Aberdeen Proving Ground, Maryland, August 1984. (AD A146568)

3. Sturek, W.B., Dwyer, H.A., and Ferry, E.N. Jr., "Prediction of In-bore and Aerodynamic Heating of KE Projectile Fins" BRL-MR-3852, U.S. Army Ballistic Research Laboratory, Aberdeen Proving Ground, Maryland, August 1990. (AD A226402)

4. Guidos, B.J., and Sturek, W.B., "Computation of Hypersonic Nosetip Heat Transfer Rates for an M829-Like Projectile" ARL-MR-52, U.S. Army Ballistic Research Laboratory, Aberdeen Proving Ground, Maryland, April 1993. (AD A2632226)

5. Bechtol, T.R., "Projectile Follower System" BRL-TR-2771, U.S. Army Ballistic Research Laboratory, Aberdeen Proving Ground, Maryland, December 1986.

6. Smith, W.J., Modern Optical Engineering, McGraw-Hill, Inc., 1966, pp. 133, 135.

7. DeWitt, D.P., and Nutter, G.D. (Editors),Theory and Practice of Radiation Thermometry, John Wiley & Sons, Inc., 1988, pp. 50, 251, 263, 329.

8. Thorman, H., and Frisk, B., "Measurement of Heat Transfer with an Infrared Camera," Int. J. Heat Mass Transfer, Vol. 11, November 1968, pp. 819-826.

9. Gartenberg, E., and Roberts, A.S.,Jr., "Phenomenological Aspects of Infrared Imaging in Aeronautical Research," AIAA Paper 88-4674, September 1988.

10. Gartenberg, E., and Roberts, A.S.,Jr., "Twenty-Five Years of Aerodynamic Research with Infrared Imaging," Journal of Aircraft, Vol. 29, No. 2, March-April 1992, pp. 161-171.

11. Nicodemus, F.E., "Normalization in Radiometry," Appl. Opt., Vol. 12, No. 12, December 1973, pp. 2960-2973.

12. Kodak High Speed Infrared Film 2481, Kodak Publication No. M-9.

13. Wyatt, C.L., Radiometric Calibration: Theory and Methods, Academic Press, Inc., 1978, pp. 67-77.

14. Vincent, J.D., Fundamentals of Infrared Detector Operation and Testing, John Wiley & Sons, 1990, pp. 279-294.

15. Kline, S.J., and McClintock, F.A., "Describing Uncertainties in Single-Sample Experiments," Mechanical Engineering, Jan. 1953, pp. 3-8.

INTENTIONALLY LEFT BLANK

6. LIST OF SYMBOLS

A	projected source area of projectile component
B_a	blur from misalignment between trajectory and rotating mirror axis
B_d	blur from diffraction
B_f	blur from defocus
B_s	blur from projectile spin
B_v	blur from velocity mismatch
BBS	blackbody simulator
D_{ts}	distance from trajectory to slit
G	collection solid angle of the rotating mirror system
$\overline{G}_a$	average system solid angle during in-flight recording
G_s	simulated solid angle used in field calibration
H_f	height of mirror facet
l_a	length of trajectory over which projectile was detected
L_b	spectral radiance of a blackbody
$P(x)$	probability density (in Figure 4), the probability of the projectile hitting within an increment dx at x divided by dx
$\Re(\lambda)$	spectral responsivity of the array detector
R	distance from the rotating mirror to the trajectory
R_a	distance realized in test shot between the rotating mirror and the trajectory
R_p	distance predicted before test shot between the rotating mirror and the trajectory
S	range from the gun
S_d	system output signal in volts or relative volts
$\overline{S}_d$	average of output signals from trajectory points
T_a	true temperature of component surface on in-flight projectile
T_b	temperature of blackbody simulator
T_c	temperature of component surface on model projectile
T_m	temperature of in-flight projectile surface as indicated by rotating mirror system
Δt	exposure time
Δt_o	obscuration time associated with transient vignetting at the mirror facet
V_a	velocity of projectile realized in test shot
V_p	velocity of projectile predicted before the test shot
V_r	velocity of projectile as measured by firing range
V_{ma}	velocity of the field of view of the rotating mirror realized in test shot
ΔV	velocity mismatch (error) between projectile velocity and velocity of the FOV of the rotating mirror

W_f width of mirror facet

W_s width of slit

x_i coordinate along trajectory

x_r reference coordinate along trajectory at which BBS is placed to get S_d vs T_b for calibration

Z distance between in-flight projectile location and plane of best focus as determined before the shot

Greek Symbols

α angle between 1) a line from a source point on the projectile surface to the spin axis and 2) a line from the system to the spin axis

β angular blur from defocus

γ angle subtended by the diffraction at the mirror facet

ε spectral directional emissivity of projectile component surface

λ wavelength

σ_p resulting standard deviation for measured signal

σ_x horizontal linear dispersion for projectile type

σ_θ horizontal angular dispersion for projectile type

$\sigma_{\Delta V}$ standard deviation associated with the velocity mismatch, ΔV

τ system spectral transmission including air path

ϕ angle giving misalignment between the axis of the rotating mirror and the normal to the plane containing the trajectory and center of the rotating mirror

Φ radiant flux in watts or photons/sec

ψ average angle of incidence between the rays in the infrared bundle arriving at the mirror facet and the facet normal

Ω angle specifying orientation of spinning projectile

ω rotation rate of mirror

ω_a actual rotation rate of mirror realized in test shot

ω_p predicted or set rotation rate of mirror before test shot

Subscripts

a actual or true value for in-flight projectile

l value in laboratory calibration

m measured value as indicated by instrument or system

p predicted value before test shot

s simulated value in field calibration

APPENDIX A

STATIC TRACER BURN TEST ON DM13 PROJECTILE TO ESTIMATE MAGNITUDE OF FIN ASSEMBLY HEATING

INTENTIONALLY LEFT BLANK

STATIC TRACER BURN TEST ON DM13 PROJECTILE TO ESTIMATE MAGNITUDE OF FIN ASSEMBLY HEATING

When a tracer burns inside a projectile fin assembly, some heating is contributed to the assembly. The issue here is whether the magnitude of heating is negligible or considerable for a particular combination of tracer and fin assembly. A literature search did not yield publications giving data about tracer heating, and therefore, the magnitude of tracer heating is presently not known to the author. To get an idea of the magnitude of the temperature rise that may result from in-flight tracer heating, a static tracer burn test was conducted on an available projectile, a DM13 kinetic energy projectile.[4]

In most projectile applications, the tracer is mounted in a cavity inside the hub of the fin assembly. It is held in place by a plug that has a thin metal seal covering an exit hole. During launch, the hot propellant gases blow through the thin metal seal and ignite the tracer. During flight, the projectile spins and the tracer cavity is subject to in-flight temperature and pressure conditions. A typical in-flight burn time is about 5 seconds.

These launch and in-flight conditions are not simulated in the following static tracer test.

A 120-mm DM13 projectile was removed from the cartridge, placed on the ground, and the tracer ignited by puncturing the metal seal at the exit hole with a nail. The tracer burned for about 9 to 10 seconds.

The temperature of the outer surface of the fin assembly was measured by viewing the assembly with an IR imager. To calibrate the video response for temperature, two blackbody simulators were viewed in the frame along with the projectile fins. The temperatures of the BBSs were 350 K and 450 K.

The surface of the fin assembly in the area surrounding the tracer cavity, after completion of the tracer burn, radiated slightly less strongly than the 450 K blackbody simulator. If the emissivity of the fin surface is about 0.9 (the surface appears to have a high emissivity "hard coat" anodized aluminum finish), the temperature of the fin assembly surface surrounding the tracer cavity would have increased about 120 K just after the completion of the tracer burn. If the emissivity is lower than 0.9, then the temperature rise would have been greater.

---

[4]The DM13 kinetic energy projectile has an aluminum fin assembly. The M865 training projectile, which was tested without tracer, has an aluminum conical base referred to as a "flare."

This test indicates that during static conditions, when a tracer burns inside the DM13 fin assembly, considerable heating occurs in the vicinity of the tracer cavity. After completion of the tracer burn, the magnitude of temperature rise is about 100 K on the outer surface of the fin hub.

The DM13 fins are made of aluminum alloy, appear "hard coated," and have walls around the tracer cavity which are about 7 mm thick. Many projectiles of more recent design have aluminum alloy fins with thinner walls surrounding the tracer cavity and therefore might experience larger temperature rises than the DM13.

APPENDIX B

THRESHOLD TEMPERATURE SCREENING TEST FOR IMAGERS

INTENTIONALLY LEFT BLANK

THRESHOLD TEMPERATURE SCREENING TEST FOR IMAGERS

The suitability of specific imagers for use in projectile imaging depends on the emissivity and temperature of the projectiles and on the spectral and absolute response of the imagers. The following screening test is useful for indicating which imagers might produce adequate signal for projectile imaging.

The objective of the screening test was to determine, using the exposure time and optical conditions used in the rotating mirror setup, the threshold temperature for workable signal levels with the IR imagers available in this laboratory. The measured threshold temperatures, along with an estimate of the expected projectile temperature and emissivity, then give an indication of the feasibility of acquiring emission images.

The test consisted of viewing a blackbody simulator (BBS) and controlling the exposure time with a chopper. The collecting aperture of the mirror facet was simulated by placing an aperture of equivalent area on the imager lens. Table B-1 lists the imagers and electronic conditions. The calibration applies to the selected conditions of electronic gain, exposure time, and collection solid angle which is given here as the f-number. The temperature of the BBS was increased in steps and the video response recorded. Figure B-1 indicates the response versus temperature for the selected exposure times and f-numbers.

There were similarities in the measured responses of all the electronic imagers. The imagers all indicate a temperature threshold below which signals are not distinguishable from noise, a range of temperature somewhat less than 200 K over which signal changes with temperature, and a "roll over" of the response curve to "saturation" where temperature increase results in little or no signal change. All imagers except the broadband pyroelectric imager can be characterized as having most of their spectral response at wavelengths below the peak of the blackbody radiance and therefore display the well-known sharp rise of output with increasing temperature [7]. It follows that the dynamic range of this type of instrumentation is limited in terms of temperature. The response curves show that once these imagers have been set up with a given exposure time and optical configuration so that the signals produced by in-flight projectiles are above noise and below saturation, the range of temperature that may be measured in a single image is narrow, roughly 200 K (for a given emissivity).

Table B-1. Imagers Tested in Screening Test

Infrared Imager	Electronic/Photographic Conditions
1. Pyroelectric Vidicon Imaging Technology Methods Corp. Model 202/PCK Lens: Coated Germanium Response Wavelength: 1.8-14 μm	Gain: As received
2. Platinum Silicide Array David Sarnoff Research Center Model IRH-32042-7 Lens: Coated Germanium Response Wavelength: 1.8-5.5 μm	Gain: 2.10 Offset: 7.60
3. PbO-PbS Vidicon Teltron, Inc Model 2500 Lens: Glass Response Wavelength: 0.9-2.5 μm	Gain: Fixed (Auto gain control disabled)
4. CCD Color Video Camera RCA Closed-Circuit Video Equipment Model TC200 (IR blocking filter removed) Lens: Glass Response Wavelength: 0.4-1.1 μm	Gain: Fixed (Auto gain control disabled)
5. Camera: Hytax Streak/Synchro-Ballistic Redlake Corporation Model 61 Lens: Glass	
Infrared Film Type 2841 Eastman Kodak Company Response Wavelength: 0.4-0.9 μm	Photographic processing: 'Pushed 2 Stops' - developed with higher temperature and extended time as recommended by manufacturer

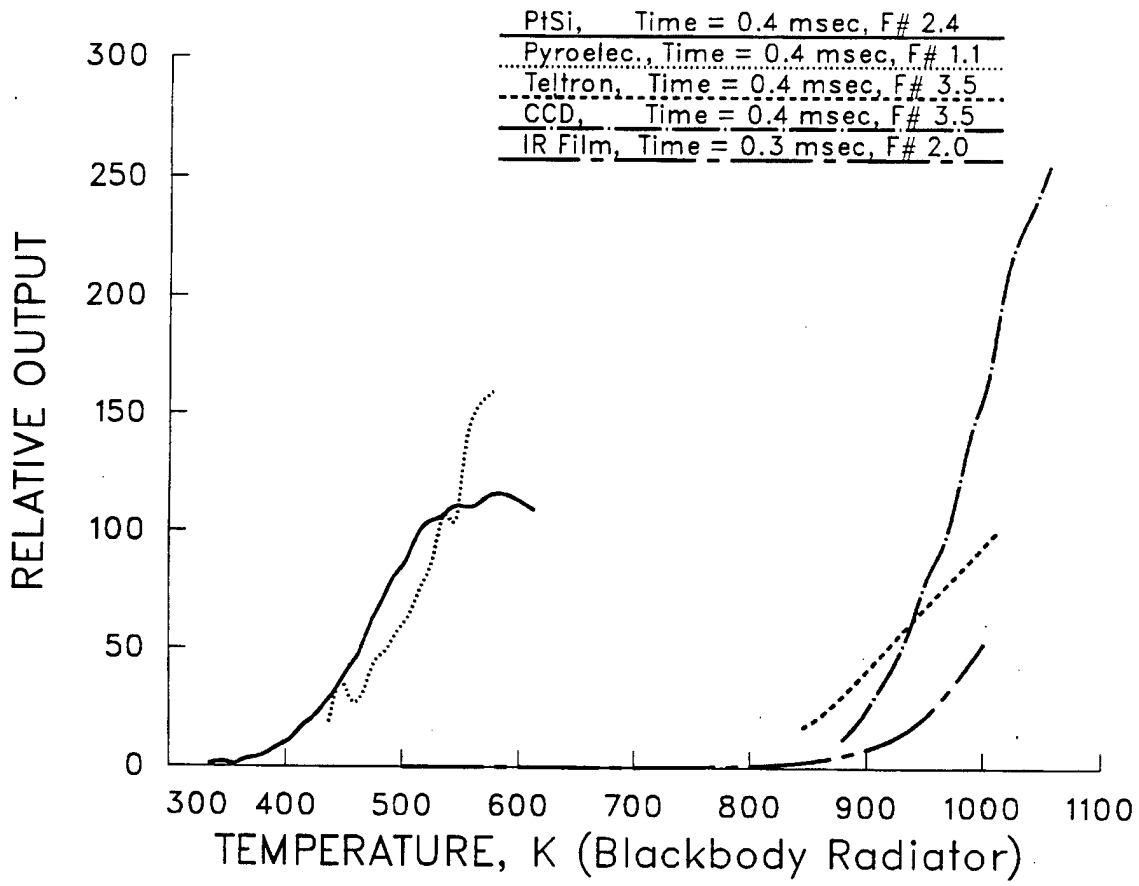

Figure B-1. System Response Versus Blackbody Temperature for Five IR Imagers. (Note, for comparison, the IR film was placed on this figure with the electronic imagers, but the response scale for the IR film is the y axis from Figure B-2.)

A measurement was also made to determine the threshold temperature required for photographic imaging with IR film, Kodak Type 2841, as used in streak/synchro-ballistic cameras commonly used on firing ranges. As a reference response for film an intermediate density of 0.3 (transmission 0.5) was selected, and the BBS temperature required to produce that response was measured. For an exposure time of 1,000 μsec and f/1.7 optics, the BBS temperature required to produce a photographic density of 0.3 was measured as 870 K. Photographed under these conditions, a blackbody at 870 K was calculated (in the wavelength response band of the film, 0.4 to 0.9 μm) to cause an energy density incident on the film of about $3x10^{-9}$ joule/cm^2. This energy density can be compared with the Kodak specification for the energy per unit area required to produce a 0.3 density response [12]. The Kodak data indicate that about $3x10^{-9}$ joule/cm^2 produces a film density of 0.3 in agreement with the $3x10^{-9}$ joule/cm^2 measured in the laboratory screening test. This energy density is plotted as a horizontal line in Figure B-2. In addition, as a rough indicator of the temperature threshold and dependence of the film response, the in-band energy per unit area produced by a blackbody as a function of temperature can be calculated. The energy densities resulting from several exposure times and f-numbers were calculated and are plotted in Figure B-2. No attempt was made to account for the variation of film response with wavelength.

A few attempts were made to photograph a KE projectile using this film in range cameras with exposure times of 300 μsec and f/2. No images were realized, presumably because no surface area on the projectile had reached about 850 K. This threshold temperature was estimated by choosing a photographic density of 0.1 as representing the minimum detectable and, by viewing Figure B-2, estimating that $1x10^{-9}$ j/cm^2 is the energy density on the film which produces a photographic density of 0.1. This minimum required energy density would have been produced by an in-flight high emissivity projectile component at a temperature of about 850 K.

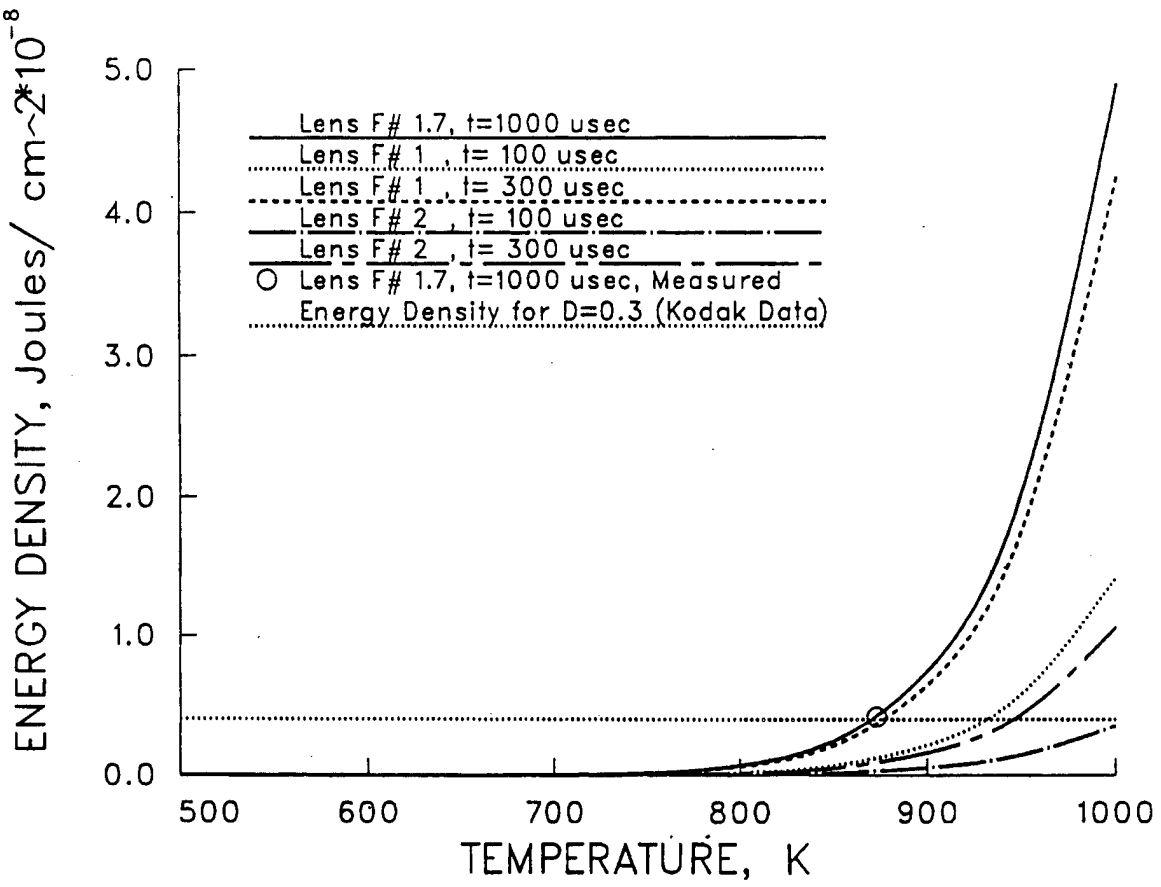

Figure B-2. Energy Density on Film Versus Blackbody Temperature. (The energy densities were calculated over 0.50 to 0.91 um, to match the response band of Kodak IR Film Type 2481.)

INTENTIONALLY LEFT BLANK

APPENDIX C

M865 PROJECTILE POST-SHOT FIELD CALIBRATION FOR RELATIVE RESPONSE ALONG TRAJECTORY

INTENTIONALLY LEFT BLANK

M865 PROJECTILE POST-SHOT FIELD CALIBRATION
FOR RELATIVE RESPONSE ALONG TRAJECTORY

Blackbody Simulator Temperature: 537 K

Trajectory Location, x_i	Video Levels & $S_d(x_i)$ = Mean		Mean/ Center Mean
- 13 cm	63 relative units[5]		
- 13 cm	62		
- 13 cm	61		
- 13 cm	59		
	Mean 61.3	$\sigma = 1.7$	87%
0 (slit center)	70		
0 (slit center)	70		
0 (slit center)	70		
0 (slit center)	72		
	Mean 70.5	$\sigma = 1.0$	-----
+ 13	77		
+ 13	76		
+ 13	74		
+ 13	69		
	Mean 74.0	$\sigma = 3.4$	105%
+ 18	71		
+ 18	69		
+ 18	70		
+ 18	69		
	Mean 69.8	$\sigma = 1.0$	99%

Comparison of averaged mean responses over four trajectory locations to mean response in center using Eq. (30):

$$\frac{\overline{G}_a}{G_s(x_r)} = \frac{\sum_{i=1}^{i=n} S_d(x_i)}{\frac{n}{S_d(x_r)}},$$

$$\frac{\overline{G}_a}{G_s(x_r)} = \frac{68.9}{70.5} = 98\%.$$

[5]Relative units are proportional to video signal voltage into 75 ohms with a conversion between 5 and 10 millivolts per relative unit.

INTENTIONALLY LEFT BLANK

APPENDIX D

ESTIMATE OF EXPERIMENTAL UNCERTAINTY IN TEMPERATURE MEASUREMENT FOR THE M865 PROJECTILE TEST

INTENTIONALLY LEFT BLANK

ESTIMATE OF EXPERIMENTAL UNCERTAINTY IN TEMPERATURE MEASUREMENT FOR THE M865 PROJECTILE TEST

The radiometric relationships were discussed in Section 2.2. In this section, the experimental uncertainty associated with measuring the in-flight projectile's surface temperature is estimated. The system is calibrated by simulating the signal from the in-flight projectile as discussed. Eq. (22) contains the component quantities that are used for the simulation: (a) exposure time, Δt_s, (b) spectral emissivity, $\varepsilon_s(\lambda)$, (c) system spectral transmission, $\tau_s(\lambda)$, and (d) collection solid angle, G_s. This section contains estimates for the component uncertainties and describes their contribution to the experimental uncertainty in measuring surface temperature for the M865 projectile test.

In this report, as discussed in Reference 15, uncertainty between two values is expressed by giving one value along with an estimated uncertainty interval. In addition, the level of confidence, or probability, of finding one value within the uncertainty interval of the other value is stated. The uncertainty interval selected here is plus or minus a standard deviation, $\pm \sigma$. With an uncertainty interval of $\pm \sigma$, it follows that one value will fall within $\pm \sigma$ of the other value with a level of confidence of 68%.[6] Standard deviations for system precision or reproducibility are calculated in Appendix C from measured values. Otherwise, the standard deviations are best estimates based on subjective judgment. σ is usually given in relative terms as a percent of the value with which it appears. The propagation of relative component uncertainties into results, as applied in this report, are discussed in Reference 15.

Using the measurement of length as an example, the uncertainty between measured length, l_m, and actual length, l_a, is expressed with the uncertainty interval of $\pm \sigma_l$, so that

$$l_m = l_a \pm \sigma_l,$$

or, stated another way,

$$l_a - \sigma_l \leq l_m \leq l_a + \sigma_l.$$

This statement of uncertainty means that l_m is estimated to fall within an interval of $\pm \sigma_l$ of l_a, with a confidence level of 68%.

[6]The probability statements (1) "with a level of confidence of 68%," as used in this report, and (2) "with odds of 2 to 1," as used in Reference 15, are nearly equivalent. That is, the statement of "odds of 2 to 1" corresponds to a confidence level of 66.7%.

1. UNCERTAINTY BETWEEN ACTUAL IN-FLIGHT EXPOSURE TIME AND POST-SHOT SIMULATED EXPOSURE TIME

In calibration, the actual exposure time is simulated by first measuring the exposure time and then setting a chopper to reproduce the measured time. Uncertainties are introduced in both steps. First, the uncertainty introduced by the measuring the exposure time is estimated.

Actual Exposure Time The actual exposure time, Δt_a, over which the in-flight M865 projectile was recorded is equal to

$$\Delta t_a = l_a / V_a, \tag{D-1}$$

in which l_a is the length of the trajectory over which the projectile was recorded and V_a is projectile velocity.

Measured Exposure Time l_a and V_a are measured, giving values l_m and V_m, which are used to find a measured exposure time, Δt_m,

$$\Delta t_m = l_m / V_m. \tag{D-2}$$

The uncertainty between the measured exposure time, Δt_m, and actual exposure time, Δt_a, results from the uncertainties in measuring length and velocity, which are discussed next.

Uncertainty in Measured Length The actual length, l_a, was measured after the shot by a visual technique similar to that described in Section 2.1 . The measured length, l_m, falls within an uncertainty interval $\pm \sigma_l$ of l_a, so that

$$l_m = l_a \pm \sigma_l.$$

The uncertainty interval for the length measurement in the M865 test is estimated as ± 10% (or in absolute terms $\pm 0.10\ l_a$), with $\sigma_l = 10\%$.

In future tests, the uncertainty between l_m and l_a could be made considerably smaller by improving the technique for estimating the trajectory length.

Uncertainty in Measured Velocity The projectile velocity is measured by firing range instrumentation and the standard deviation, σ_V, between the measured projectile velocity, V_m, and actual velocity, V_a, is estimated as 0.5%, so that

$$V_m = V_a \pm \sigma_V,$$

with

$$\sigma_V = 0.5\%.$$

Uncertainty in Measured Exposure Time The component uncertainties for l_m and V_m, when used in Eq. (D-2), propagate into the result to give an uncertainty in Δt_m with standard deviation of

$$\sigma_{\Delta tm} = [\sigma_l^2 + \sigma_V^2]^{1/2},$$

$$\sigma_{\Delta tm} = 10\%.$$

Then, the uncertainty between the measured and actual exposure times is

$$\Delta t_m = \Delta t_a \pm 10\%. \qquad \text{(D-3)}$$

Uncertainty in Chopper Simulated Exposure Time Next in the calibration procedure, the measured exposure time was reproduced by placing a chopper in front of a blackbody simulator. This chopper time is the simulated exposure time of Eq. (22), Δt_s. The uncertainty between the chopper simulated exposure time, Δt_s, and the measured exposure time, Δt_m, is estimated as ± 5% of Δt_m and expressed as

$$\Delta t_s = \Delta t_m \pm \sigma_{\Delta ts},$$

with

$$\sigma_{\Delta ts} = 5\%.$$

Uncertainty Between Simulated and Actual Exposure Times Combining the effects of the uncertainties in first measuring the exposure time and then setting the chopper pulse time, the resulting standard deviation between the simulated exposure time, Δt_s, and the actual exposure time, Δt_a, is estimated as

$$\sigma_{\Delta t} = [\sigma_{\Delta tm}^2 + \sigma_{\Delta ts}^2]^{1/2},$$

$$\sigma_{\Delta t} = 11\%.$$

Finally, the uncertainty between the simulated exposure time and actual exposure time is

$$\Delta t_s = \Delta t_a \pm 11\%. \tag{D-4}$$

that is, the simulated exposure time is estimated to fall within an interval of ± 11% (or in absolute terms $\pm 0.11\Delta t_a$) of actual exposure time with a level of confidence of 68%.

For example, if the actual exposure time were 200 μsec, then this exposure time could be measured to within ± 10% and the chopper could be operated to produce pulses within ± 5% of the measured time. Then, the resulting uncertainty between the simulated exposure time and the actual exposure time of 200 μsec is ± 11% or ± 22 μsec.

2. UNCERTAINTY BETWEEN ACTUAL IN-FLIGHT EMISSIVITY AND MODEL-SIMULATED EMISSIVITY

The uncertainty between the actual component spectral emissivity, $\varepsilon_a(\lambda)$, of the in-flight projectile and the corresponding spectral emissivity, $\varepsilon_s(\lambda)$, of the oven model, in which the in-flight projectile and oven model are from the same manufacturing lot, is subjectively estimated as

$$\varepsilon_s(\lambda) = \varepsilon_a(\lambda) \pm \sigma_\varepsilon,$$

with

$$\sigma_\varepsilon = 5\%.$$

3. UNCERTAINTY BETWEEN ACTUAL SYSTEM TRANSMISSION AND SIMULATED TRANSMISSION

The spectral transmission of the system affects the signals produced in the field and laboratory. The rotating mirror was used in three setups for different purposes:

1. in-flight recording
2. field calibration
3. laboratory measurement

The same optical components were used in each setup. Differences in the broadband air path absorption over these short paths (6 meters in the field and 3 meters in the laboratory) are negligible. Therefore, the spectral transmissions for each setup are considered unchanged. Then, the uncertainty between the simulated and actual spectral transmissions is

$$\tau_s(\lambda) = \tau_a(\lambda) \pm \sigma_\tau,$$

with

$$\sigma_\tau \approx 0.$$

4. SINGLE SAMPLE UNCERTAINTY ASSOCIATED WITH OBSERVING SOURCE WITH IMAGER AND READOUT

The imager and readout were applied to a highly reproducible source, that is, the chopped BBS as measured in Appendix C, and the reproducibility of the system and source together were estimated by the standard deviation of the observed values. It is assumed that the reproducibility of the BBS source does not have a large influence on the observed signals and that the distribution of observed values is solely the result of the system's measurement reproducibility. From Appendix C, the largest standard deviation observed in a series of measurements at any of the four trajectory locations was $\sigma < 5\%$ at location +13 cm. Using this largest observed standard deviation as a conservative estimate, the standard deviation for the system's reproducibility is estimated as

$$\sigma_i = 5\%.$$

Assuming the signals have a normal distribution, the standard deviation gives the reproducibility of the signals when the system is used to view highly reproducible sources, that is, sources with much better reproducibility than the system. In the projectile application, the above standard deviation would be expected in a population of signals if repeated measurements were made on projectiles with identical surfaces and temperatures. In real tests, since the individual projectiles have emissivity and temperature variations, the signals would have a larger distribution.

The standard deviation can also be applied to estimate the probability that the signal recorded in a single in-flight projectile experiment will lie within a specified value from the true value [15]. For example, the probability that a single projectile test will yield a signal value within one standard deviation, or ± 5% of the true value, is 68%. A single measurement would lie within two standard deviations, or ± 10%, 95% of the time and within three standard deviations, or ± 15%, 99.7% of the time, etc.

5. UNCERTAINTY BETWEEN ACTUAL AVERAGE SOLID ANGLE FOR THE IN-FLIGHT RECORDING AND SIMULATED SOLID ANGLE USED IN CALIBRATION

During the in-flight test, the IR photons emitted by the projectile were collected by the system with an average solid angle of $\overline{G}_a$ steradians. Since the system's instantaneous collection solid angle may vary along the trajectory, $\overline{G}_a$ must be estimated after the shot by measuring the relative responses at sample points along the trajectory as discussed in Section 2.2.2. The mean values for signals at each point, labeled $S_d(x_i)$, are averaged to yield a post-shot measurement for $\overline{G}_a$. How well the solid angle used in calibration, G_s, simulates $\overline{G}_a$, is evaluated by using Eq. (30)

$$\frac{\overline{G}_a}{G_s(x_r)} = \frac{\dfrac{\sum_{i=1}^{i=n} S_d(x_i)}{n}}{S_d(x_r)}.$$

The uncertainty between G_s and $\overline{G}_a$ would normally be estimated by using standard deviations from the sampled points, such as those in Appendix C, and examining their effect on computing the average in Eq. (30). However, for this M865 test, as mentioned in Section 2.2.3, the uncertainty was increased because two of the trajectory points closest to the slit edges were not sampled during the field calibration procedure. Next, the increased uncertainty caused by taking the average from just four trajectory points instead of six points is estimated.

Take x_1 and x_6 to be the trajectory points at which measurements were not taken and x_2, x_3, x_4, and x_5 to be the four points at which measurements were taken. The measured means from the four points appear in Appendix C and are identified here as $S_d(x_2)$, $S_d(x_3)$, $S_d(x_4)$ and $S_d(x_5)$.

The increased uncertainty can be estimated by considering the bundle of light from the facet and examining how it enters the lens for sources at the two unmeasured points. The vignetting of the light bundle by the lens aperture is discussed in Section 2.2.1 and shown in Figure 2. For a source at one of the unmeasured points, the lens edge may have blocked the bundle more than at the four measured points. However, because the bundle progressively translates across the lens, the added vignetting may have occurred at one but not at both of the unmeasured trajectory points.

Some assumptions are now made to estimate limits for the missing signals:

1. For the unmeasured point with the most vignetting, for example, point x_1, it is assumed that, $S_d(x_1)$, if measured, would have yielded a value no worse than between zero and the average, $\bar{S}_d$, of the four measured points, that is, the average of $S_d(x_2)$, $S_d(x_3)$, $S_d(x_4)$ and $S_d(x_5)$. With limits of

$$0 < S_d(x_1) < \bar{S}_d.$$

2. For the other unmeasured point with the least vignetting, for example, point x_6, it is assumed that, if measured, $S_d(x_6)$ would have yielded a value no worse than between the average and twice the average of the four measured points. With limits of

$$\bar{S}_d < S_d(x_6) < 2\bar{S}_d.$$

These limits for the signals are unlikely to be reached, given the degree of vignetting, and therefore overestimate the error. For example, for the signal to be zero, the edge of the lens has to completely block the light bundle.

The worst case combinations given the above limits are

1. For the measurement at the most vignetted point to equal the average and for the measurement at the least vignetted point to equal twice the average,

$$S_d(x_1) = \bar{S}_d \quad \text{and} \quad S_d(x_6) = 2\bar{S}_d.$$

In this case, the true average of six measurements would be about 17% higher than the average of the four measurements.

2. For the measurement at the most vignetted point to equal zero and for the measurement at the least vignetted point to equal the average,

$$S_d(x_1) = 0 \quad \text{and} \quad S_d(x_6) = \bar{S}_d.$$

In this case, the true average is about 17% lower than the average of the four measurements.

The uncertainty between the average measured by the four points and the average that would have resulted if six points had been measured, is estimated using the limits and worst case combinations as ± 17%. This uncertainty in knowing the true average, when used in Eq. (30), results in an equivalent uncertainty between G_s and $\bar{G}_a$.

The uncertainty between the simulated collection solid angle, G_S, and the actual average collection solid angle, $\overline{G}_a$, is estimated as ± 17%,

$$G_S = \overline{G}_a \pm \sigma_G,$$

with

$$\sigma_G = 17\%.$$

This estimate probably overestimates the uncertainty interval. In future tests, with more complete measurements across the slit opening, the uncertainty between $\overline{G}_a$ and G_S, the largest component uncertainty in the M865 test simulation, would be considerably smaller.

While measuring at only four points instead of six adds uncertainty, when the operation of the rotating mirror as used in the M865 test is considered, it seems reasonable that the increase is not large. The mirror rotation angle was very small, about 2°, and the corresponding translation of the bundle of light rays entering the lens was also small. When the source moved from a measured point to the adjacent unmeasured point with vignetting, for example, from x_2 to x_1 in the above example, the translation was only about 1 millimeter. The system's aperture without vignetting is the cross section of the bundle from the facet. As shown on Figure 2, the cross section of the bundle is relatively wide (nearly 30 mm) and therefore, a 1-millimeter translation will not cause enough additional vignetting to change the system's aperture or solid angle very much.

6. RESULTING UNCERTAINTY BETWEEN ACTUAL IN-FLIGHT SIGNAL AND SIMULATION SIGNAL CAUSED BY THE ABOVE COMPONENT UNCERTAINTIES

The signal produced by the in-flight projectile is simulated to calibrate the system for temperature. There is an uncertainty between the signal produced by the in-flight projectile and the signal produced by the simulation. This uncertainty results from the component uncertainties in Δt_s, ε_s, and G_s of Eq. (22) plus the system's reproducibility uncertainty, $\pm \sigma_i$, as estimated above. The resulting uncertainty between the signal produced by the simulation and that from the in-flight projectile is

$$S_d(T_c) = S_d(T_a) \pm \sigma_s,$$

with

$$\sigma_s = \sqrt{\sigma_{\Delta t}^2 + \sigma_\varepsilon^2 + \sigma_G^2 + \sigma_i^2},$$

$$\sigma_s = \sqrt{(11\%)^2 + (5\%)^2 + (17\%)^2 + (5\%)^2},$$

$$\sigma_S = 21\%.$$

That is, the signal produced by the post-shot simulation with the oven model will fall within ± 21% (or in absolute terms ± $0.21S_d(T_a)$) of the signal produced by the in-flight projectile (when both are at the same temperature) with a confidence level of 68%. For the M865 test, the uncertainties in simulated exposure time and collection solid angle were larger than necessary because of the preliminary nature of these measurements.

7. EXPERIMENTAL UNCERTAINTY FOR TEMPERATURE MEASUREMENT IN THE M865 PROJECTILE TEST

Thermal radiation is characterized by a very strong dependence of radiance on temperature. As an example, for a blackbody at temperature, T, if the emission is detected across a wavelength band that is below the wavelength of peak radiance (as in this application), the in-band radiance goes as T^y in which $y > 5$ [7].

Because of the strong dependence of radiance on temperature, the above uncertainty of ± 21% in signal level leads to only a small temperature error. The temperature error associated with an uncertainty in the system's output signal can be seen by referring to Figure 11 and considering the effect of a ± 21% uncertainty in signal on reading the temperature. For the mid-scale video levels on the curve, an uncertainty of ± 21% in the signal level corresponds to a temperature uncertainty of only about ± 15 K or ± 3% of the absolute temperature. At the high or low ends of the curve, the temperature uncertainties will be greater and are not estimated here. The uncertainty between the component temperature of the oven model and the component temperature on the in-flight projectile when both produce the same signal is

$$T_c = T_a \pm \sigma_{T_S},$$

with

$$\sigma_{T_S} = 15 \text{ K}.$$

The analysis of experimental uncertainty so far has covered the uncertainties in the calibration procedures associated with the simulated values and the system's reproducibility. At this point, the unknown temperature, T_a, of the in-flight projectile has been calibrated, in effect, against the known temperature, T_c, of a reference source, the oven model.

However, another uncertainty is now added because the true temperature of the oven model is not known exactly. The oven model is heated to a temperature indicated by a thermocouple attached to the model. The temperature of the oven model is highly reproducible as indicated by observing the thermocouple. However, because the temperature on the outer surface may differ

from the thermocouple reading, a systematic error or bias may be introduced. The uncertainty associated with both the precision and any bias of the oven model are considered together to give a standard deviation like estimate. The uncertainty in the surface temperature, T_c, of the oven model is subjectively estimated at ± 16 K,

$$T_m = T_c \pm \sigma_{T_c},$$

with

$$\sigma_{T_c} = 16 \text{ K}.$$

That is, the measured surface temperature of the oven model, as indicated by the thermocouple, will be within ± 16 K of true surface temperature with a 68% level of confidence. In future laboratory tests, this uncertainty could be made smaller by more accurately determining any bias between the thermocouple temperature and the surface temperature of the component of the oven model.

The standard deviation that results from combining the uncertainty of ± 15 K associated with the calibration procedures and the uncertainty of ± 16 K in knowing the true component temperature of the oven model is

$$\sigma_T = \sqrt{\sigma_{T_s}^2 + \sigma_{T_c}^2},$$

$$\sigma_T = \sqrt{(15)^2 + (16)^2},$$

$$\sigma_T = 22 \text{ K}.$$

Finally, for the tail flare component on the in-flight M865 projectile as presented in Figure 12, the uncertainty between the measured temperature, T_m, and the true surface temperature, T_a, is

$$T_m = T_a \pm 22 \text{ K}.$$

That is, the measured temperature is estimated to be within an uncertainty interval of ± 22 K of the true temperature with a level of confidence of 68%. This estimate applies to any video level within the range that is displayed by the color red in Figure 12.

NO. OF
COPIES ORGANIZATION

2 ADMINISTRATOR
DEFENSE TECHNICAL INFO CENTER
ATTN DTIC DDA
8725 JOHN J KINGMAN RD STE 0944
FT BELVOIR VA 22060-6218

1 DIRECTOR
US ARMY RESEARCH LABORATORY
ATTN AMSRL OP SD TA/ RECORDS MGMT
2800 POWDER MILL ROAD
ADELPHI MD 20783-1197

1 DIRECTOR
US ARMY RESEARCH LABORATORY
ATTN AMSRL OP SD TL/TECH LIB
2800 POWDER MILL ROAD
ADELPHI MD 20783-1197

1 DIRECTOR
US ARMY RESEARCH LABORATORY
ATTN AMSRL OP SD TP/TECH PUB BR
2800 POWDER MILL ROAD
ADELPHI MD 20783-1197

ABERDEEN PROVING GROUND

5 DIRECTOR
US ARMY RESEARCH LABORATORY
ATTN AMSRL OP AP L (TECH LIB)
BLDG 305 APG AA

34 DIRECTOR
US ARMY RESEARCH LABORATORY
ATTN AMSRL-SC-I W STUREK
AMSRL-SC-CC C NIETUBICZ
AMSRL-SE-RM H B WALLACE
AMSRL-SL-BV J RAPP
AMSRL-WT D ECCLESHALL
AMSRL-WT-W C H MURPHY
AMSRL-WT-PC R BEYER
AMSRL-WT-PB M BUNDY
J GARNER
B GUIDOS
P PLOSTINS
E SCHMIDT
K SOENCKSEN
P WEINACHT
AMSRL-WT-WB F BRANDON
L BURKE
AMSRL-WT-WD P BERNING
R BOSSOLI
S CORNELISON

NO. OF
COPIES ORGANIZATION

AMSRL-WT-WD A GAUSS
C HOLLANDSWORTH
C HUMMER
L KECSKES
T KOTTKE
M MCNEIR
A NIILER
J POWELL
A PRAKASH
D STRENZWILK
C STUMPFEL (5 CYS)
G THOMSON

1 US ARMY TECOM
ATTN AMSTE TM T J SCHNELL
RYAN BLDG